


Electron-phonon coupling induced topological phase transition in an α - T_3 Haldane-Holstein modelMijanur Islam¹,* Kuntal Bhattacharyya¹,† and Saurabh Basu[‡]*Department of Physics, Indian Institute of Technology Guwahati, Guwahati-781039, Assam, India* (Received 18 April 2024; revised 29 June 2024; accepted 2 July 2024; published 15 July 2024)

We present compelling evidence of topological phase transitions induced by electron-phonon (e-ph) coupling in an α - T_3 Haldane-Holstein model that facilitates smooth tunability between graphene ($\alpha = 0$) and a dice lattice ($\alpha = 1$). The e-ph coupling has been incorporated via the Lang-Firsov transformation which adequately captures the polaron physics in the high-frequency (anti-adiabatic) regime, and yields an effective Hamiltonian through zero phonon averaging at $T = 0$. While exploring the signature of phase transitions driven by polaron and its interplay with the parameter α , we identify two regions based on the values of α , namely, the low to intermediate range ($0 < \alpha \leq 0.6$) and larger values of α ($0.6 < \alpha < 1$), where the topological transitions host distinct behavior. There exists a single critical e-ph coupling strength for the former, below which the system behaves as a topological insulator characterized by edge modes, finite Chern number, and Hall conductivity, with all of them vanishing above this value, and the system undergoes a spectral gap closing transition. Further, the critical coupling strength depends upon α . For the latter case ($0.6 < \alpha < 1$), the scenario is more interesting where there are two critical values of the e-ph coupling at which trivial-topological-trivial and topological-topological-trivial phase transitions occur. Our study shows a significant difference with regard to the well-known unique transition occurring at $\alpha = 0.5$ (or at 0.7) in the absence of the e-ph coupling, and thus underscores the importance of interaction effects on topological phase transitions.

DOI: [10.1103/PhysRevB.110.045426](https://doi.org/10.1103/PhysRevB.110.045426)**I. INTRODUCTION**

Upsurge in generating the topological phases in condensed matter systems has been a modern trend for the last few decades [1,2]. Although the concept of topology has been prevalent in mathematics for a long time back, it gained enormous attention in modern condensed matter systems thanks to the pioneering work by Thouless *et al.* [3]. The TKNN formalism serves as the fundamental tool for understanding the topological nature associated with the quantized plateaus of the quantum Hall (QHE) [4] systems. In the subsequent years, the interest in predicting new topological phases remains unabated in two [5,6] and three [7–10] dimensions, topological semimetals [11,12], topological superconductors [13], and many more. Moreover, with the discovery of symmetry-protected topological phases in such systems, a continuous phase transition can be realized between states with same symmetry but different topology, has led to the study of exotic topological materials [1,2,14,15]. The topological properties of these phases are protected against disorder. Owing to such robustness to external perturbations, these systems offer potential applications in modern quantum devices, such as quantum computers etc.

Apart from the QHE observed in the presence of an external magnetic field, there have been efforts to realize similar behavior even in the absence of a magnetic field [16–19].

It was first claimed by Haldane [20] that a complex next-nearest neighbor (NNN) hopping with a phase ϕ (also called as the Haldane flux) in a two-dimensional honeycomb lattice breaks the time-reversal symmetry (TRS) of the system and the bands are indexed by a topological invariant, known as the Chern number which is analogous to the quantization of the Hall conductivity. Furthermore, the inclusion of a staggered Semenoff mass (M) term in such systems results in the breaking of the sublattice symmetry, which is responsible for opening and closing a band gap at the Dirac points (commonly denoted by the K and K' points) in the Brillouin zone (BZ).

Of late, the study of topology in multiband systems has emerged as one of the fundamental areas that has reshaped the overall scenario of modern condensed matter physics [21–30]. With the advent of two-dimensional (2D) graphene-like materials, immense interest has been drawn to studying electronic and transport properties in honeycomb lattices and its variants [31,32]. Unlike bare graphene, where the electronic properties are characterized by the Dirac quasiparticles in the low-energy limit, there exists a variant of the honeycomb lattice with T_3 symmetry, known as the T_3 or the dice lattice [33–45], where the low-energy spectrum of the lattice is governed by the Dirac-Weyl quasiparticles. The T_3 lattice exhibiting pseudospin $S = 1$ states can be thought of as an extension to the bare graphene (pseudospin $S = 1/2$), fabricated by an additional atom at the center of the hexagon and may be visualized as comprising of a “C” sublattice as shown in Fig. 1.

It has been proposed that the dice lattice can be realized in a cold-atom experimental setup by three counter-propagating laser beams [40]. Furthermore, the realization of such lattice is proposed by growing a heterostructure consisting of a trilayer

*Contact author: mislam@iitg.ac.in†Contact author: kuntalphy@iitg.ac.in‡Contact author: saurabh@iitg.ac.in

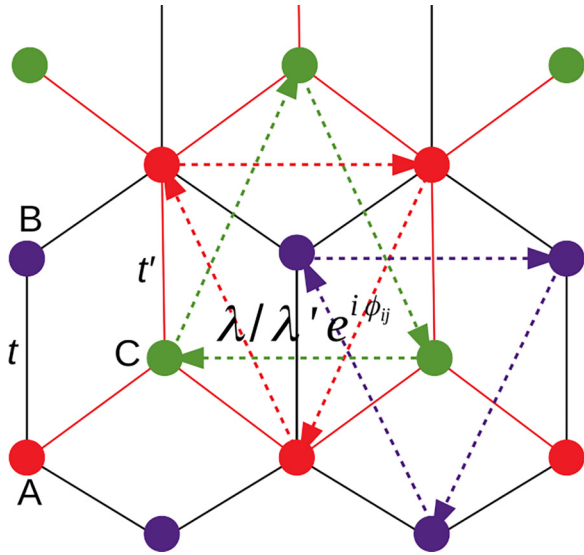


FIG. 1. The schematic diagram of an α - T_3 lattice is shown, where the red, purple, and green circles represent the sublattices A, B, and C sublattices, respectively. The NN hopping strength between A and B sublattices (solid black line) is t , while it is $t' = \alpha t$ between A and C sublattices (solid red line). The NNN hopping between A-B-A (dashed red) or B-A-B (dashed purple) is $\lambda e^{i\phi_{ij}}$, while through C, it is $\lambda' e^{i\phi_{jk}}$ between A-C-A (dashed red) and C-A-C (dashed green). Here $\lambda' = \alpha\lambda$ and the phase ϕ_{ij} ($-\phi_{ij}$) denotes the clockwise (anticlockwise) direction.

of cubic lattices, namely, SrTiO₃/SrIrO₃/SrTiO₃ in the (111) direction [41]. Interestingly, a smooth transformation from pseudospin $S = 1/2$ state to pseudospin $S = 1$ can be apprehended using a more generalized version of the T_3 system, known as the α - T_3 lattice [46–49], where α is the strength of the nearest neighbor (NN) hopping from the central atom (shown by the red line in Fig. 1). Therefore an α - T_3 lattice sets the two extreme limits, namely, $\alpha = 0$ (graphene) and $\alpha = 1$ (dice), between which a continuous control is possible by parametrizing α suitably through a variation of the Berry phase, proportional to α . Raoux *et al.* [46] have explored the role of the Berry phase in α - T_3 lattice and shown that the orbital susceptibility of the system undergoes a transition from a diamagnetic ($\alpha = 0$) to a paramagnetic ($\alpha = 1$) at a critical $\alpha_c = 0.495$ while the Berry phase changes from π (graphene) to 0 (dice). Due to the presence of the additional atom at the center, the low-energy spectrum of the α - T_3 lattice, governed by the tight-binding Dirac-Weyl Hamiltonian, embodies two dispersive bands that are linear in momenta and a dispersionless flat band at zero-energy. Malcolm *et al.* [47] have shown that the bulk dispersion of a quantum well structure made of Hg_{1-x}Cd_xTe can be linked to the low-lying dispersion of an α - T_3 lattice with an effective $\alpha = 1/\sqrt{3}$ at a critical Cd doping concentration, $x_c \approx 0.17$. In recent times, such α - T_3 lattices with enlarged spin states ($S > 1/2$) have offered a series of studies on equilibrium [44–70] and nonequilibrium [71–77] properties. To highlight a few, people have investigated the role of Berry phase [46,48,56,71,77], valley-polarized transport [52,74] that may be applicable to valleytronics, Klein tunneling [53], optical conductivity

[48,51,58–60,64], magnetotransport properties, such as the Shubnikov–de Hass oscillation and quantized Hall conductivity [48,50,54,56], Floquet dynamics [72,75], Majorana corner states [45], and other topological signatures [37,43,44,49] in α - T_3 or dice lattices. As there was evidence in the past which demonstrated the topology of the multiband systems, such as, kagomé [25,27,28], Lieb [30], and dice [35,37,39,41] lattices could be turned into a Chern insulator by tuning the system parameters, recently, Dey *et al.* [72] have attempted to show the topological transition at a critical $\alpha_c = 1/\sqrt{2}$ via irradiating an α - T_3 lattice with a circularly polarized light.

However, the role of many-body correlations like electron-electron and electron-phonon interactions in inducing the topological phase transition in an α - T_3 lattice is left unnoticed. To the best of our knowledge, the previous proposals of topological phase transition are mainly in noninteracting systems (single-particle picture) where the topology is solely described by the properties of the bands of the electron [37,43,49,78] or by other external means [58,72]. Nevertheless, attempts were made to investigate the topological phase transitions driven by many-body interactions in the past [26,44,45,79–88], most of which are devoted to explaining the effects of electronic correlations on the topological phases of matter. On the contrary, the role of electron-phonon (e-ph) interaction in such contexts has been scarce. Historically, the e-ph interaction has been proven to deliver promising discoveries in solids [89–91] starting from the inducing superconductivity [92–94], transport in three-dimensional materials [95], low-dimensional polaronic effects [96–100], Peierls transition [101–104], charge density wave [105–113] formation in solids to the Fermi polarons in ultracold gases [114–117], topological signatures in novel systems [118–121], etc. More recently, Bose polaron [122–125], phonon-induced Floquet topological phases [126,127] and several others have been actively explored. In a polar or an ionic crystal, a propagating electron distorts the lattice structure. Consequently, a net polarization potential emerges due to the interaction between the electron and the ‘oscillating’ lattice because of which the electron itself may get trapped. The quasiparticles generated because of this interaction can be identified as electrons dressed with phonon clouds, which are commonly known as polarons. Depending on the strength of the e-ph interaction, the polarons can be self-trapped (strong coupling limit) or delocalized (weak coupling limit). In a tight binding system, the electron is found to be strongly bound to its own lattice site, and that electron can participate in forming the polaron by interacting with the onsite phonons. Therefore the radius of the polaron in such narrow-band systems is short-ranged and does not spread over many lattice sites. The polarons in such systems are often called as the small polarons or the Holstein polarons [128,129]. The polaron formation in tight binding systems can be realized through an interaction between the “extra” fermionic impurity and the phonons in the system. We shall include the “polaron” physics in a nontrivially gapped system. As discussed earlier, breaking the TRS via complex NNN hopping is a starting point for our study. Specifically, we assume that this “impurity” moving in the α - T_3 lattice and interacting with the lattice vibrations, gives rise to the nontrivial spectral gap arises by polarons formed in a Haldane Chern insulator.

The main focus of this paper is whether e-ph interaction in such a Haldane-Holstein model on an α - T_3 lattice can induce topological phase transitions. If yes, whether these transitions are accompanied by the conventional wisdom, such as (dis)appearance of conducting edge modes, abrupt change in the topological invariant, the behavior of the anomalous Hall conductivity etc. This interaction-driven topology may provide a favorable platform to explore exotic phenomena in the topological materials. It also serves to connect the correlated phenomena in physics with topology. There are a few studies which describe the importance of e-ph coupling in determining the nontrivial phases in the Haldane Chern insulator [130,131], graphene nanoribbons [132], topological superconductivity [133], and in other two-dimensional materials [88,132,134–136]. Cangemi *et al.* [130] have proposed a topological quantum transition in a Haldane Chern insulator driven by the e-ph coupling, where they have shown the system undergoes a nontrivial to trivial transition with increasing e-ph coupling strength, where the average number of fermions shows a sharp discontinuity at the transition point indicating a topological transition. Along the same line, Camacho *et al.* [131] have calculated a phonon-induced transverse Hall effect through the “composite Berry phase” and shown the conductance jumps from zero to a finite value accompanied by a nonzero Chern number. Using a diagrammatic technique in the continuum Dirac model, Pimenov *et al.* [134] have reported a similar observation as in Ref. [131]. These studies largely encourage looking for systems that exhibit a nontrivial phase and possible phase transitions upon suitably tuning the strength of the e-ph coupling.

However, there is hardly any study revealing the effects of e-ph interaction for an α - T_3 system in the presence of a topological gap. Therefore, in this study, we aim to explore the role of e-ph coupling in stimulating the nontrivial topological phases in the α - T_3 lattice, which may provide a fruitful prescription to understand the interaction-driven topology in other novel systems.

The remainder of this paper is organized in the following manner. In Sec. II, we describe our system and present the model Hamiltonian of a polaronic α - T_3 lattice, which is written in Sec. II A under the framework of the Haldane model modified by a Holstein term accounting for the e-ph coupling. In Sec. II B, we show the polaron formation in our system employing the Lang-Firsov technique, which works well for the high-frequency (anti-adiabatic) optical phonons. Section II C deals with the momentum space representation of the model Hamiltonian, which we shall use to calculate the band spectra and topological quantities. Section III is devoted to studying the topological phase transition driven by polarons, where we present our numerical results of the bulk and edge spectra in Secs. III A and III B, respectively, while interpolating between graphene and a dice structure. In these sections, we discuss how the bulk bands behave and, consequently, the appearance of the edge state and their vanishing below and above a particular critical e-ph coupling strength as a function α . The results will imply a plausible occurrence of topological phase transitions. In Sec. III C, we confirm the topological transitions induced by polaron via numerically computing the polaronic Chern number and the Berry curvature. The results show the discontinuous jumps in the Chern number diagram at

critical values of the e-ph coupling that depend on α . Further proof, such as the quantized Hall plateaus below the critical value of e-ph coupling obtained in Sec. III D also signifies the topological transition driven by e-ph interaction in our system. Finally, in Sec. IV, we conclude our results and briefly summarize our findings.

II. α - T_3 LATTICE WITH ELECTRON-PHONON INTERACTION

The α - T_3 lattice is schematically shown in Fig. 1. Each hexagon of the lattice constituting A (red), B (purple), and C (green) lattice site forms the unit cell of an α - T_3 lattice where A and B atoms construct the regular honeycomb (graphene) lattice with NN hopping strength t and C is considered to be the additional atom placed at the center of each hexagon connected only to the A atoms via a hopping strength αt ($\alpha \leq 1$). The hopping between a C and a B atom is prohibited. We introduce our model Hamiltonian below in the presence of an e-ph interaction.

A. Haldane-Holstein model for α - T_3 lattice

We formulate our system in the spirit of a tight-binding Haldane-Holstein Hamiltonian, which is written as

$$\begin{aligned} \mathcal{H} = & \left[-t \sum_{\langle i,j \rangle} c_i^\dagger c_j - \alpha t \sum_{\langle j,k \rangle} c_j^\dagger c_k - \frac{\lambda}{3\sqrt{3}} \sum_{\langle\langle i,j \rangle\rangle} e^{i\phi_{ij}} c_i^\dagger c_j \right. \\ & \left. - \frac{\alpha\lambda}{3\sqrt{3}} \sum_{\langle\langle j,k \rangle\rangle} e^{i\phi_{jk}} c_j^\dagger c_k + \text{H.c.} \right] + M \sum_i c_i^\dagger S_z c_i \\ & + \hbar\omega_0 \left[\sum_i \left(b_i^\dagger b_i + \frac{1}{2} \right) + \lambda_{\text{eph}} \sum_i c_i^\dagger c_i (b_i^\dagger + b_i) \right], \end{aligned} \quad (1)$$

where $c_{i,j,k}^\dagger (c_{i,j,k})$ denotes the electronic creation (annihilation) operator corresponding to A, B, and C sites with i , j , and k indices, respectively. The first term represents the NN hopping between the A and B sites with hopping amplitude t , while the second one stands for that between the A and C sites with a different amplitude $t' = \alpha t$, which is present due to the C atoms of a typical α - T_3 lattice. We denote the NN terms by a single angular bracket, $\langle \dots \rangle$. The third term is the Haldane term designated for the next nearest-neighbor (NNN) complex hoppings (denoted by the double angular bracket $\langle\langle \dots \rangle\rangle$) between A-B-A or B-A-B with an amplitude λ and a phase ϕ_{ij} , where it is ϕ_{ij} ($-\phi_{ij}$) when the motion of the electron is clockwise (anticlockwise). The effect of the C-atoms in the NNN A-C-A and C-A-C hoppings is represented by the fourth term with a different strength, $\lambda' = \alpha\lambda$. Therefore the two limiting cases of our study are the results for graphene ($\alpha = 0$) and dice ($\alpha = 1$) lattices. The fifth term of Eq. (1) is the Samenoff mass term, M is the mass, and S_z is the z component of the pseudospin-1 matrix. The effects of phonon modes are incorporated in the sixth and seventh terms, where the sixth term is the total onsite energy of the phonons denoted by the phononic creation (annihilation) operators, $b_i^\dagger (b_i)$ of site i and the last term of this modified Haldane model is the Holstein term that describes the onsite coupling between

electrons and the longitudinal optical (LO) phonons with a coupling strength λ_{eph} , $\hbar\omega_0$ being the energy scale of phonons with a dispersionless LO frequency, ω_0 .

B. Polaronic Hamiltonian: Lang-Firsov approach

The quasiparticles formed by the interaction between a bosonic lattice field (a phonon) and a fermionic charge carrier (an electron) undergo emission and absorption of virtual phonons by the electrons at $T = 0$. Owing to such an interaction, a net polarization potential is generated in which the electrons may get trapped. These quasiparticles dressed with virtual phonon clouds are known as polarons. For a tight-binding system, the size of a polaron is usually less compared to the lattice constant and is known as a small Holstein polaron. Here, we have only considered the onsite e-ph interaction, and neglecting the interactions of electrons

with the NN and NNN site phonons, these being weak enough. To study the effects of the e-ph coupling, we first employ the much celebrated Lang-Firsov transformation (LFT), namely,

$$\tilde{\mathcal{H}} = e^R \mathcal{H} e^{-R}, \quad (2)$$

where the generator of the transformation is given by [137]

$$R = \lambda_{\text{eph}} \sum_i c_i^\dagger c_i (b_i^\dagger - b_i). \quad (3)$$

This is a coherent transformation of a displaced harmonic oscillator that eliminates the phonon degrees of freedom and transforms the Hamiltonian into that for an effective electronic system. We must specify that this unitary transformation works well in the high-frequency (non-adiabatic) regime, meaning the LO frequency of the phonons is much larger than the other electronic parameters of the system, i.e., when $\omega_0 \gg t, t', \lambda, \lambda', M$ and λ_{eph} . The LFT transforms the total Hamiltonian (1) as (see Appendix for the derivation)

$$\begin{aligned} \tilde{\mathcal{H}} = & -t \left[\sum_{\langle i,j \rangle} c_i^\dagger c_j e^{[X_i - X_j]} + \alpha \sum_{\langle j,k \rangle} c_j^\dagger c_k e^{[X_j - X_k]} \right] - \frac{\lambda}{3\sqrt{3}} \left[\sum_{\langle\langle i,j \rangle\rangle} e^{i\phi_{ij}} c_i^\dagger c_j e^{[X_i - X_j]} + \alpha \sum_{\langle\langle j,k \rangle\rangle} e^{i\phi_{jk}} c_j^\dagger c_k e^{[X_j - X_k]} \right] \\ & + \sum_i c_i^\dagger (MS_z - \lambda_{\text{eph}}^2 \hbar\omega_0 I_3) c_i + \hbar\omega_0 \sum_i b_i^\dagger b_i, \end{aligned} \quad (4)$$

where I_3 is a 3×3 identity matrix.

The X terms in the exponent contain the phonon operators as

$$X_i = \lambda_{\text{eph}} (b_i^\dagger - b_i). \quad (5)$$

At this stage, to eliminate the phonon degrees of freedom, one can obtain a zero-phonon average (at $T = 0$), which reads for the exponents as

$$\langle 0 | e^{[X_i - X_j]} | 0 \rangle = e^{-\lambda_{\text{eph}}^2}, \quad (6)$$

The quantity in RHS of Eq. (6) is known as the Holstein reduction factor which causes the band narrowing. The last term in Eq. (4) becomes zero after zero-phonon averaging. Therefore, in the transformed Hamiltonian (4), all the parameters are modified by the e-ph coupling and the effective Hamiltonian becomes

$$\begin{aligned} \tilde{\mathcal{H}}_{\text{eff}} = \langle 0 | \tilde{\mathcal{H}} | 0 \rangle = & -\tilde{t} \left[\sum_{\langle i,j \rangle} c_i^\dagger c_j + \alpha \sum_{\langle j,k \rangle} c_j^\dagger c_k \right] \\ & - \frac{\tilde{\lambda}}{3\sqrt{3}} \left[\sum_{\langle\langle i,j \rangle\rangle} e^{i\phi_{ij}} c_i^\dagger c_j + \alpha \sum_{\langle\langle j,k \rangle\rangle} e^{i\phi_{jk}} c_j^\dagger c_k \right] \\ & + \sum_i c_i^\dagger (MS_z - \lambda_{\text{eph}}^2 \hbar\omega_0 I_3) c_i, \end{aligned} \quad (7)$$

where the reduced Holstein and Haldane amplitudes are renormalized as

$$\tilde{t} = t e^{-\lambda_{\text{eph}}^2}, \quad \tilde{\lambda} = \lambda e^{-\lambda_{\text{eph}}^2}. \quad (8)$$

It is clear from Eq. (7) that the signatures of polaron in our system are captured through \tilde{t} and $\tilde{\lambda}$ (both contain λ_{eph}). As e-ph interaction modifies system parameters, it will be interesting to see how polaron induces a topological phase transition at certain critical e-ph coupling strength. To investigate the same, we need to transform the Hamiltonian (7) to the momentum (\mathbf{k}) space and calculate the band structures along with the relevant topological properties.

C. Continuum α - T_3 -Holstein Hamiltonian

The modified \mathbf{k} -space version of an α - T_3 lattice in the presence of e-ph interaction can be obtained by Fourier transforming the effective Haldane-Holstein Hamiltonian (7) in a triatomic sublattice basis as

$$\begin{aligned} \tilde{\mathcal{H}}(\mathbf{k}) = & -\tilde{t} (h_x S_x + h_y S_y) - \frac{2\tilde{\lambda} \Im(f_{\mathbf{k}})}{3\sqrt{3} \cos \varphi} S_{zH} \\ & + MS_z - \lambda_{\text{eph}}^2 \hbar\omega_0 I_3, \end{aligned} \quad (9)$$

with

$$\begin{aligned} S_x = & \begin{pmatrix} 0 & \cos \varphi & 0 \\ \cos \varphi & 0 & \sin \varphi \\ 0 & \sin \varphi & 0 \end{pmatrix}, \quad S_y = -i \begin{pmatrix} 0 & \cos \varphi & 0 \\ -\cos \varphi & 0 & \sin \varphi \\ 0 & -\sin \varphi & 0 \end{pmatrix}, \\ S_z = & \begin{pmatrix} 1 & 0 & 0 \\ 0 & 0 & 0 \\ 0 & 0 & -1 \end{pmatrix}, \quad S_{zH} = \begin{pmatrix} -\cos \varphi & 0 & 0 \\ 0 & \cos \varphi - \sin \varphi & 0 \\ 0 & 0 & \sin \varphi \end{pmatrix}, \end{aligned} \quad (10)$$

where S_x and S_y are the x and y components of the pseudospin-1 matrix written in terms of an angle φ which is related to the parameter α as $\varphi = \tan^{-1} \alpha$. Specifically, S_{zH} arises due to the presence of the NNN Haldane term. The parameter $\nu = \pm 1$ denote the valleys K and K' located at $K = (4\pi/3\sqrt{3}a, 0)$ and $K' = (-4\pi/3\sqrt{3}a, 0)$. The polaronic contributions to Eq. (9) enter through \tilde{t} , $\tilde{\lambda}$ [defined in Eq. (8)] and the last term in Eq. (9). h_x , h_y , and $f_{\mathbf{k}}$ in Eq. (9) are given as

$$h_x = \sum_{i=1}^3 \cos(\mathbf{k} \cdot \mathbf{d}_i), \quad h_y = \sum_{i=1}^3 \sin(\mathbf{k} \cdot \mathbf{d}_i), \quad (11)$$

$$f_{\mathbf{k}} = \sum_{i=1}^3 e^{i(\mathbf{k} \cdot \mathbf{a}_i)}, \quad (12)$$

$$\tilde{\mathcal{H}}(\mathbf{q}) = \hbar \tilde{v}_f \begin{pmatrix} M - \lambda_{\text{eph}}^2 \hbar \omega_0 & (vq_x - iq_y) \cos \varphi & 0 \\ (vq_x + iq_y) \cos \varphi & -\lambda_{\text{eph}}^2 \hbar \omega_0 & (vq_x - iq_y) \sin \varphi \\ 0 & (vq_x + iq_y) \sin \varphi & -M - \lambda_{\text{eph}}^2 \hbar \omega_0 \end{pmatrix} - \frac{\tilde{\lambda} \nu}{\cos \varphi} \begin{pmatrix} -\cos \varphi & 0 & 0 \\ 0 & \cos \varphi - \sin \varphi & 0 \\ 0 & 0 & \sin \varphi \end{pmatrix}, \quad (13)$$

with $\hbar \tilde{v}_f = 3a\tilde{t}/2 \cos \varphi$ and $\mathbf{q} = (q_x, q_y) = \mathbf{k} - K$ or $(\mathbf{k} - K')$.

It is well known that the Dirac-Weyl Hamiltonian (13) represents two dispersive bands, namely the valance band (VB) and the conduction band (CB), along with a dispersionless flat band (FB) for graphene ($\alpha = 0$) and dice ($\alpha = 1$) lattices, and a distorted FB for $0 < \alpha < 1$ [49]. In our case, all of these are modified by the polaronic factors through \tilde{t} and $\tilde{\lambda}$ defined in Eq. (8).

III. POLARON INDUCED TOPOLOGICAL FEATURES IN AN α - T_3 LATTICE

In this section, we present the numerical results of our system and study the effects of e-ph interaction in the context of topological phase transition.

A. Bulk spectral properties

In our study, all the energy parameters are taken in units of t , which is set to unity. Further, we fix $a = 1$ (lattice constant), $\phi_{ij} = \pi/2$ (the Haldane flux), and $\hbar = 1$, for convenience.

Before delving into the specifics of the e-ph interaction, let us briefly explore the bare Haldane α - T_3 lattice. In the absence of e-ph interaction and the mass term, and solely due to the breaking of the time-reversal symmetry by the Haldane term, the original zero-energy FB may get distorted. Additionally, the electronic band structure experiences valley splitting. Figure 2 illustrates the low-energy bands for various values of α within the first BZ. The red, green, and blue colors denote the CB, FB, and VBs, respectively. In three-band systems, there can be two distinct band gaps at the Dirac points: the gaps between (i) the CB and the distorted FB ($\Delta_{cf}^{K/K'}$) and (ii) the distorted FB and VBs ($\Delta_{vf}^{K/K'}$) at the K/K' points. The middle band exhibits no dispersion at $\alpha = 0$ (not depicted here), but it gets more dispersive with increasing α . We see a mild dispersive nature of the FB at $\alpha = 0.4$ as shown in Fig. 2(a). In Fig. 2(b), where $\alpha = 0.5$, the distorted FB now connects with the VB by closing the gap between them at

where the coordinates of the NN sites are $\mathbf{d}_1 = (\sqrt{3}a/2, a/2)$, $\mathbf{d}_2 = (-\sqrt{3}a/2, a/2)$, and $\mathbf{d}_3 = (0, -a)$, while that of the NNN sites are $\mathbf{a}_1 = (\sqrt{3}a/2, 3a/2)$, $\mathbf{a}_2 = (-\sqrt{3}a/2, 3a/2)$, and $\mathbf{a}_3 = (\sqrt{3}a, 0)$, a being the lattice constant. Henceforth, we shall use the \mathbf{k} -space Haldane-Holstein Hamiltonian in Eq. (9) extensively for the rest of the paper.

To obtain the low-energy limit of the above Bloch Hamiltonian, we must expand Eq. (9) in the vicinity of the Dirac points around K and K' valleys and linearize it which takes the form of a pseudospin-1 Dirac-Weyl Hamiltonian for the polaronic α - T_3 lattice as

the K valley, while in the other valley (K'), the distorted FB connects to the CB. With further increase in α , the gap reopens, as depicted in Fig. 2(c) for $\alpha = 0.6$. In case of $\alpha = 1$ (not shown here), the spectral gap attains its maximum value, and the distorted FB regains its dispersionless behavior. Notably, at $\alpha = 0.5$ one finds that, $\Delta_{cf}^K \neq 0$, but $\Delta_{vf}^K = 0$, and further $\Delta_{cf}^{K'} = 0$, whereas $\Delta_{vf}^{K'} \neq 0$. These findings precisely correspond with the previously reported results concerning the α - T_3 lattice [49,72]. Let us include e-ph interaction in the ongoing discussion. We set the mass as $M = 0.05t$, NNN hopping as $\lambda = 0.1t$ and the phonon frequency as $\omega_0 = 3t$ which is greater than t, M, λ for nonadiabaticity to be valid. In order to study the topological phases and transitions therein,

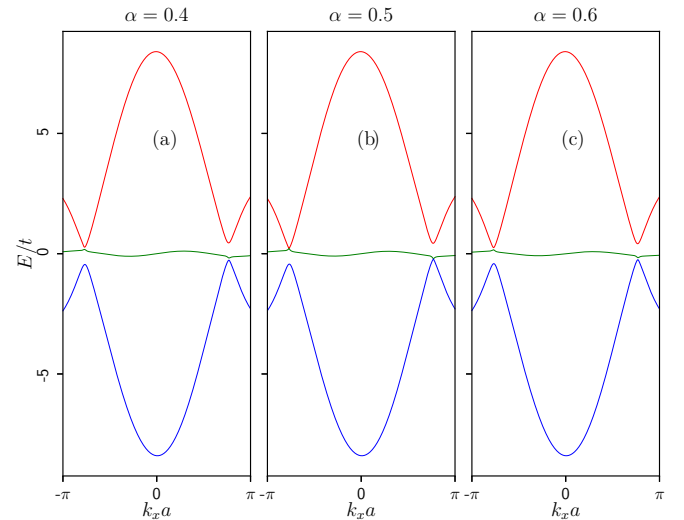


FIG. 2. The bulk band structures with energy E (in the units of t) of the bare Haldane model are shown as a function of dimensionless momenta, k_x (multiplied by the lattice constant) at $k_y = 0$ for various values of α : (a) $\alpha = 0.4$, (b) 0.5 , and (c) 0.6 . The red, green, and blue colors represent the CB, FB, and VBs, respectively. Bands are no longer symmetric under the exchange of valleys (K and K'). The Haldane term is taken as $\lambda = 0.1t$.

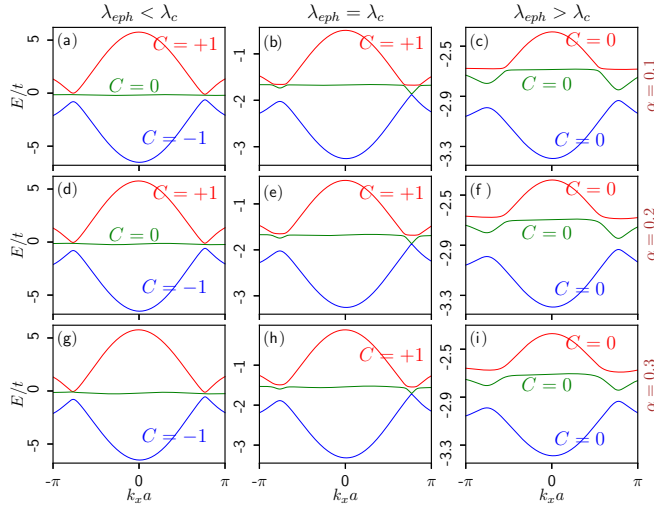


FIG. 3. Plots of polaronic bulk band structure with energy E (in the units of t) for lower α values are shown as a function of dimensionless momenta, k_x (multiplied by the lattice constant) at $k_y = 0$. (Left column) The dispersions are plotted in the $\lambda_{\text{eph}} < \lambda_c$ regime for (a) $\alpha = 0.1$, (d) 0.2, and (g) 0.3, at $\lambda_{\text{eph}} = \lambda_c$ (middle column) Those are plotted at the critical $\lambda_{\text{eph}} (= \lambda_c)$ for (b) $\alpha = 0.1$, $\lambda_c = 0.49$; (e) $\alpha = 0.2$, $\lambda_c = 0.48$; and (h) $\alpha = 0.3$, $\lambda_c = 0.47$. (Right column) The same are shown in the $\lambda_{\text{eph}} > \lambda_c$ regime for (c) $\alpha = 0.1$, (f) 0.2, and (i) 0.3, at $\lambda_{\text{eph}} = 0.6$. The red, green, and blue colors represent the CB, FB, and VBs, respectively. The parameters are taken as $\lambda = 0.1t$ and $M = 0.05t$. Further, t and λ values are modified as \tilde{t} and $\tilde{\lambda}$ as mentioned in the text. The Chern number, C (calculated in Sec. III C) corresponding to each band (however, ill-defined for those exhibiting zero bulk gap) is shown. The values of λ_c are mentioned in Table I.

we first present the bulk spectrum of the α - T_3 system for a few chosen values of α in Fig. 3 and examine the closing and opening of bulk gaps at the valleys via tuning the e-ph interaction strength λ_{eph} . As the bulk properties vary with the parameter α , we segregate them into two classes of α , namely, (i) $0 < \alpha \lesssim 0.6$ (from close to the bare graphene to moderate α cases), (ii) $0.6 \lesssim \alpha < 1$ (from moderate α to Dice lattice). The purpose of such distinction will be clear in a moment. First of all, in Fig. 3, we show the bulk energy bands for lower α values, namely, for $\alpha = 0.1, 0.2$, and 0.3 . As expected, we get three different spectra, namely, the VB (shown in blue), the FB (in green), and the CB (in red) as a function of the dimensionless momentum $k_x a$ (k_y is set to be zero). The FBs are dispersive (especially for $\alpha > 0$ cases)

TABLE I. Table of λ_c points for α in the range $0.1 < \alpha \leq 0.6$.

α	λ_c
0.1	0.49
0.2	0.48
0.3	0.47
0.4	0.46
0.5	0.45
0.6	0.43

due to the presence of the NNN hopping λ . Further, we notice a semi-Dirac dispersion, i.e., linear along k_y and quadratic along the k_x direction. The variations of the bands are shown in three different regimes of λ_{eph} , i.e., when $\lambda_{\text{eph}} < \lambda_c$ (left panel), at $\lambda_{\text{eph}} = \lambda_c$ (middle panel), and then when $\lambda_{\text{eph}} > \lambda_c$ (right panel), where λ_c is the critical e-ph coupling strength at which the gap closing ($\Delta_{\text{vf}}^K = 0$) occurs. These critical points (λ_c) for different α values are listed in Table I and the corresponding plot is shown in the inset (b) of Fig. 14(i).

Let us consider the $\alpha = 0.1$ case [Figs. 3(a)–3(c)]. As mentioned earlier, the mass term lifts the valley degeneracy. Also, the overall band spectrum is shifted vertically down as we increase λ_{eph} further (the FB not being at $E = 0$). Interestingly, at the two valleys, K and K' , the e-ph interaction makes the behavior of the FBs contradictory (which otherwise looks symmetric when $\lambda_{\text{eph}} = 0$ (see Fig. 2), especially at $\lambda_{\text{eph}} = \lambda_c$ points. We clearly notice that in the $\lambda_{\text{eph}} < \lambda_c$ regime [Fig. 3(a)], the FB almost touches the CB at both the K and K' valleys. Although, a prominent gap between VB and FB is maintained in the $\lambda_{\text{eph}} < \lambda_c$ regime. However, as soon as λ_{eph} reaches a critical value, i.e., when $\lambda_{\text{eph}} = \lambda_c = 0.49$, the FB touches the VB [Fig. 3(b)] at one of the valleys (K) and the band gap closes ($\Delta_{\text{vf}}^K = 0$), while at the other valley (K'), the spectrum remains gapped ($\Delta_{\text{vf}}^{K'} \neq 0$). The band gap re-opens and the gap persists if we increase λ_{eph} further. Beyond λ_c ($\lambda_{\text{eph}} > \lambda_c$), the behavior of the FB is almost similar at both the valleys [Fig. 3(c)], especially for larger values of α . Therefore, both in $\lambda_{\text{eph}} < \lambda_c$ and $\lambda_{\text{eph}} > \lambda_c$ regimes, the spectrum remains gapped, implying it to be an insulator, and at $\lambda_{\text{eph}} = \lambda_c$ the bands touch, signifying a semimetallic (SM) behavior. We need to compute the topological properties for different λ_{eph} regimes to confirm the topological nature of the phase, which we shall show in the later sections (Secs. III B and III C). This phenomenon of band closing and opening at the Dirac points may give rise to a topological phase transition that is solely caused by tuning the e-ph interaction strength. This is the central result of the paper. Smaller values of α in the range $[0.1 : 0.3]$ demonstrate similar behavior (Fig. 3) with different λ_c 's (listed in Table I).

The intermediate α cases ($0.4 \leq \alpha \leq 0.6$) are shown in Fig. 4 where we observe the same phenomena, except that one notices for $\alpha = 0.6$ case, the FB and VB nearly touch each other even when $\lambda_{\text{eph}} < \lambda_c$ [the values of λ_c are mentioned in Table I] region (can be seen clearly if we zoom in Fig. 4(g)). This feature persists for larger values of α ($\alpha > 0.6$) and it needs to be addressed carefully. To do so, we plot the band structure in Fig. 5 for $\alpha = 0.7$, where it is clearly shown that the VB and the FB touch each other below a certain critical value, namely, $\lambda_{c1} = 0.28$ which may describe an SM phase in the $\lambda_{\text{eph}} < \lambda_{c1}$ regime [Fig. 5(b)] and will hold even when $\lambda_{\text{eph}} = 0$ [Fig. 5(a)]. Then, in the vicinity of $\lambda_{\text{eph}} = \lambda_{c1}$, the gap between VB and FB opens for the first time [can be seen clearly in the inset of Fig. 5(c)], signaling an insulating behavior, and the gap stays intact in the $\lambda_{c1} < \lambda_{\text{eph}} < \lambda_{c2}$ regime [can be seen clearly in the inset of Fig. 5(d)] up to a second critical point, namely, $\lambda_{c2} = 0.43$, at which the gap closes [Fig. 5(e)], referring a reonset of an SM phase. The bulk spectrum is gapped beyond λ_{c2} [Fig. 5(f)]. For $\alpha = 0.8$ and 0.9 , the scenario is a bit more interesting. Unlike $\alpha = 0.7$, for

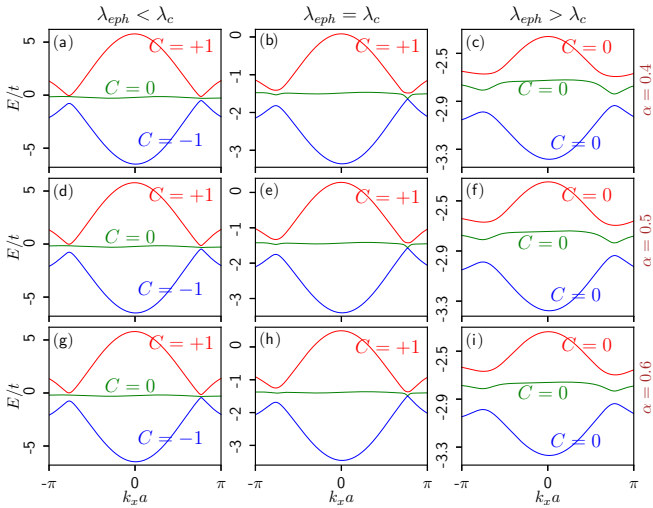


FIG. 4. Plots of polaronic bulk band structure with energy E (in the units of t) for intermediate α values are shown as a function of dimensionless momenta, k_x (multiplied by the lattice constant) at $k_y = 0$. (Left column) The dispersions are plotted in the $\lambda_{\text{eph}} < \lambda_c$ regime for (a) $\alpha = 0.4$, (d) 0.5, and (g) 0.6, at $\lambda_{\text{eph}} = 0.3$. (Middle column) Those are plotted at the critical $\lambda_{\text{eph}} (= \lambda_c)$ for (b) $\alpha = 0.4$, $\lambda_c = 0.46$; (e) $\alpha = 0.5$, $\lambda_c = 0.45$; and (h) $\alpha = 0.6$, $\lambda_c = 0.43$. (Right column) The same are shown in the $\lambda_{\text{eph}} > \lambda_c$ regime for (c) $\alpha = 0.4$, (f) 0.5, and (i) 0.6, at $\lambda_{\text{eph}} = 0.6$. The red, green, and blue colors represent the CB, FB, and VBs, respectively. The parameters are taken as $\lambda = 0.1t$ and $M = 0.05t$. Further, t and λ values are modified as \tilde{t} and $\tilde{\lambda}$ as mentioned in the text. The values of λ_c are mentioned in Table I.

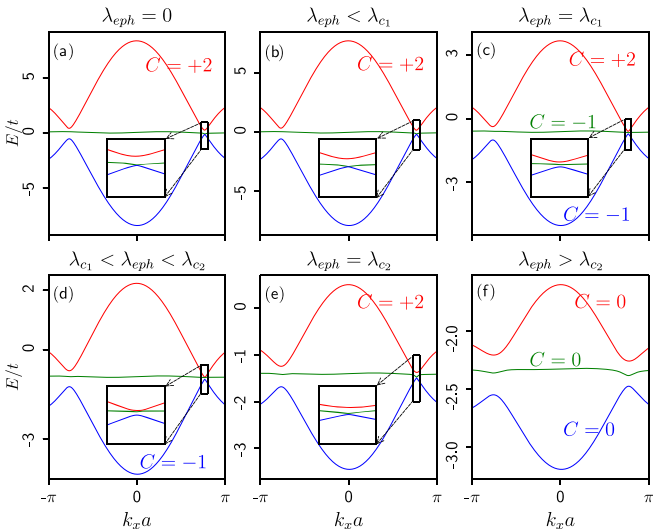


FIG. 5. Plots of polaronic bulk band structure with energy E (in the units of t) for $\alpha = 0.7$ are shown as a function of dimensionless momenta, k_x (multiplied by the lattice constant) at $k_y = 0$ for (a) $\lambda_{\text{eph}} = 0$, (b) $\lambda_{\text{eph}} < \lambda_{c1}$ ($\lambda_{\text{eph}} = 0.2$), (c) $\lambda_{\text{eph}} = \lambda_{c1} = 0.28$, (d) $\lambda_{c1} < \lambda_{\text{eph}} < \lambda_{c2}$ ($\lambda_{\text{eph}} = 0.35$), (e) $\lambda_{\text{eph}} = \lambda_{c2} = 0.43$, and (f) $\lambda_{\text{eph}} > \lambda_{c2}$ ($\lambda_{\text{eph}} = 0.6$). The red, green, and blue colors represent the CB, FB, and VBs, respectively. In the insets, a zoomed in view of the regions near the band minima (Dirac) point is shown. The parameters are taken as $\lambda = 0.1t$ and $M = 0.05t$. Further, t and λ values are modified as \tilde{t} and $\tilde{\lambda}$ as mentioned in the text. The values of λ_{c1} and λ_{c2} are mentioned in Table II.

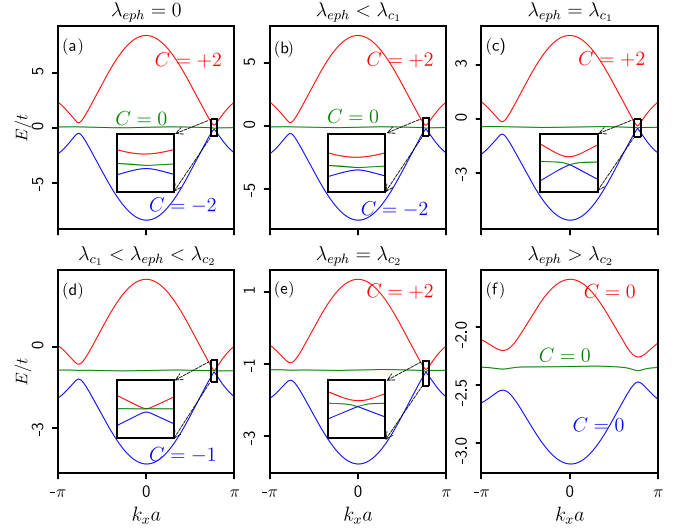


FIG. 6. Plots of polaronic bulk band structure with energy E (in the units of t) for $\alpha = 0.8$ are shown as a function of dimensionless momenta, k_x (multiplied by the lattice constant) at $k_y = 0$ for (a) $\lambda_{\text{eph}} = 0$, (b) $\lambda_{\text{eph}} < \lambda_{c1}$ ($\lambda_{\text{eph}} = 0.15$), (c) $\lambda_{\text{eph}} = \lambda_{c1} = 0.2$, (d) $\lambda_{c1} < \lambda_{\text{eph}} < \lambda_{c2}$ ($\lambda_{\text{eph}} = 0.35$), (e) $\lambda_{\text{eph}} = \lambda_{c2} = 0.44$, and (f) $\lambda_{\text{eph}} > \lambda_{c2}$ ($\lambda_{\text{eph}} = 0.6$). The red, green, and blue colors represent the CB, FB, and VBs, respectively. In the insets, a zoomed in view of the regions near the band minima (Dirac) point is shown. The parameters are taken as $\lambda = 0.1t$ and $M = 0.05t$. Further, t and λ values are modified as \tilde{t} and $\tilde{\lambda}$ as mentioned in the text. The values of λ_{c1} and λ_{c2} are mentioned in Table II.

$\alpha = 0.8$, we observe in Figs. 6(a) and 6(b) that the bulk bands remain gapped (can be seen clearly in the insets) in $\lambda_{\text{eph}} < \lambda_{c1}$ regime (including $\lambda_{\text{eph}} = 0$), signifying an insulating (not SM as for $\alpha = 0.7$) phase till $\lambda_{\text{eph}} = \lambda_{c1} = 0.2$, where the FB and VB touch each other for the first time [Fig. 6(c)] and the insulating to SM transition takes place. As we tune λ_{eph} above λ_{c1} , we observe the same phenomena as it is shown for $\alpha = 0.7$ case (Fig. 5), that is, in $\lambda_{c1} < \lambda_{\text{eph}} < \lambda_{c2}$ regime [Fig. 6(d)], the FB and VB remain gapped (can be seen clearly in the insets) denoting an insulating phase till $\lambda_{\text{eph}} = \lambda_{c2} = 0.44$ at which the system again shows a SM [Fig. 6(e)] nature and for $\lambda_{\text{eph}} > \lambda_{c2}$ [Fig. 6(f)] it behaves like an insulator, alike it does for $\alpha = 0.7$ case. Similar observations hold for $\alpha = 0.9$ (not shown here). The values of λ_{c1} and λ_{c2} for 0.7, 0.8, and 0.9 are listed in Table II. We wish to mention that for $0.8 \leq \alpha < 1$, this feature of multiple phase transition becomes more prominent as we approach the dice lattice ($\alpha = 1$). Therefore, for higher α cases ($\alpha > 0.6$), we encounter two situations, one is for $0.6 < \alpha < 0.8$ and another is for $0.8 \leq \alpha < 1$. In the former case, we get two critical λ_c points, namely, λ_{c1} and λ_{c2} , below (even when $\lambda_{\text{eph}} = 0$) and above which the system

TABLE II. Table of λ_{c1} and λ_{c2} points for higher values of α .

α	λ_{c1}	λ_{c2}
0.7	0.28	0.43
0.8	0.20	0.44
0.9	0.26	0.39

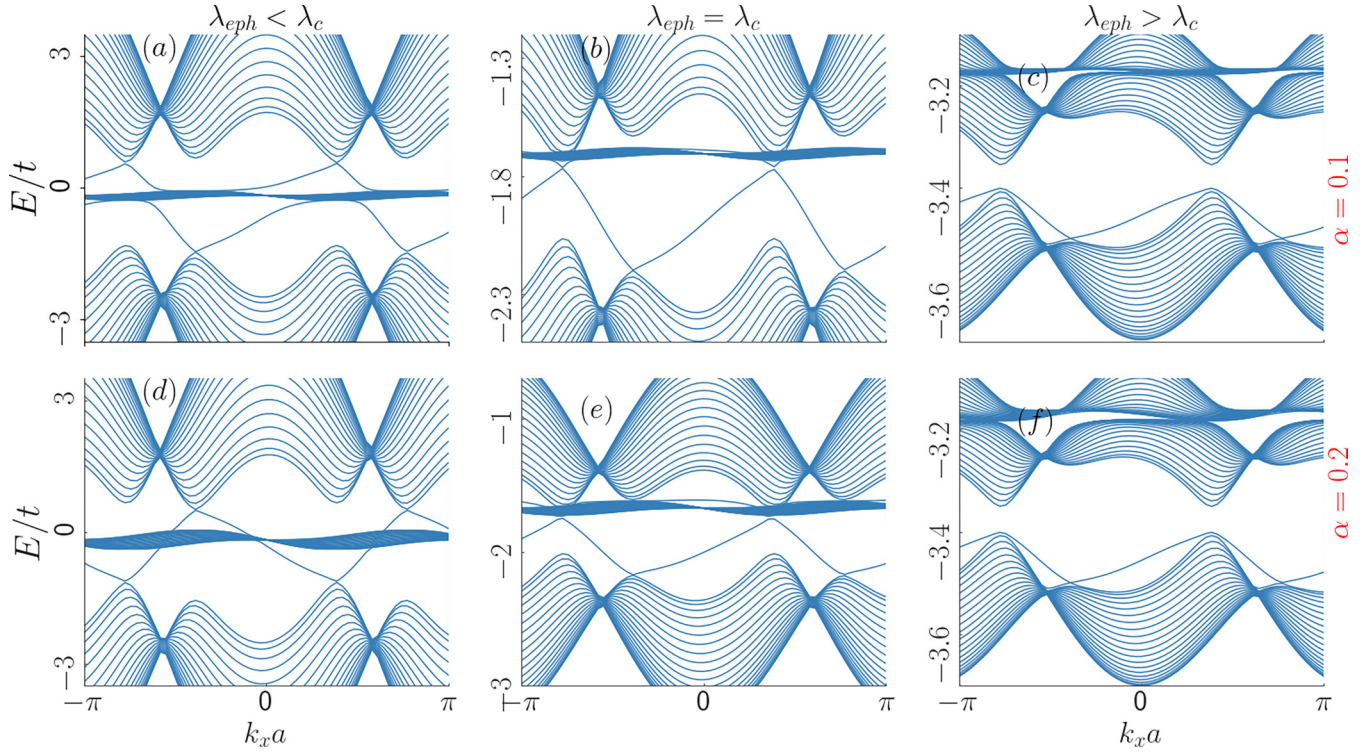


FIG. 7. Energy spectra (in units of t) of the edge states are shown for a zigzag edged semi-infinite ribbon as a function of dimensionless momenta, k_x (multiplied by the lattice constant) of $\alpha = 0.1$ for (a) $\lambda_{\text{eph}} = 0.3$ ($\lambda_{\text{eph}} < \lambda_c$), (b) $\lambda_{\text{eph}} = \lambda_c = 0.49$, and (c) $\lambda_{\text{eph}} = 0.6$ ($\lambda_{\text{eph}} > \lambda_c$), and of $\alpha = 0.2$ for (d) $\lambda_{\text{eph}} = 0.3$ ($\lambda_{\text{eph}} < \lambda_c$), (e) $\lambda_{\text{eph}} = \lambda_c = 0.48$, and (f) $\lambda_{\text{eph}} = 0.6$ ($\lambda_{\text{eph}} > \lambda_c$). Other parameters are the same as those in Fig. 3. The values of λ_c are mentioned in Table I.

respectively remains semi-metallic and insulating respectively. In between λ_{c1} and λ_{c2} , it behaves like an insulator. So, the system undergoes an SM-insulator-SM-insulator transition in the former case, while in the latter case, the system inherits an insulator-SM-insulator-SM-insulator transition. The nature of the gap (topological or trivial), will be ascertained in Secs. III B and III C. Hence, the band topology in our study is substantially modified by the polaron formation, which is governed by two factors: the renormalized amplitudes \tilde{t} and $\tilde{\lambda}$ [Eq. (8)] and also the interplay between MS_z and $\lambda_{\text{eph}}^2 \hbar \omega_0$ [last two terms of Eq. (9)]. The former causes the band narrowing and the latter is responsible for the competitive effects between the mass term and the polaron shift energy. Moreover, these polaronic markers make the variations of the band spectra (especially those of the FB and VBs) different for different ranges of α . Specifically, for higher values of α , the correlation between M , α , and λ_{eph} becomes stronger, giving rise to multiple phase transitions. In the case of the dice lattice ($\alpha = 1$), the flat band remains flat without any distortion and there is no occurrence of band gap closing phenomena for any values of the e-ph coupling λ_{eph} (not shown here). So, no λ_{eph} yields a topological phase transition. It is worth mentioning that the values of λ_c are different for different α cases (see Tables I and II), which ensures that we shall have a phase transition for all α values between $\alpha = 0$ to 1, albeit with different λ_c values.

It may be a good idea to introduce an indexing scheme of the bulk bands presented in Figs. 3–6. As our Hamiltonian is devoid of the basic symmetry, such as time reversal (owing to the complex second neighbor hopping), inversion (due to the

Samenoff mass), etc., we are left with indexing the bands by their topological invariant, namely, the Chern number (calculated in Sec. III C).

B. Edge modes of a semi-infinite α - T_3 ribbon

In this section, to provide support to the topological properties, we discuss the edge state characteristics of a semi-infinite α - T_3 ribbon in the presence of e-ph coupling. In order to envisage whether the bulk band gap is topologically nontrivial, we inspect the crossings of the edge modes between CB and VB through the FB. The ribbon geometry is considered to exhibit zigzag edges [138]. Thus it is infinite along the x direction, while finite along the y direction, breaking the translational symmetry along one direction (k_y in this case), while the same is protected along the other direction (k_x). We have taken the width of the nanoribbon as $N = 37$, which satisfies the condition of width $N = 3q + 1$ (q is an integer), and ensures both the edges are composed of A and C sublattices only. The nontrivial topological signatures are reflected in the edge state spectrum, and the details depend upon the values of α . We begin by referring to Fig. 7, where we show the edge states for lower α values ($\alpha = 0.1$ and 0.2 marked on the right edge). As stated above in Sec. III A, the bulk gap closes at a critical λ_c and it remains gapped corresponding to $\lambda_{\text{eph}} < \lambda_c$ and $\lambda_{\text{eph}} > \lambda_c$. We wish to ascertain the existence of edge states that distinguishes a topologically nontrivial phase from a trivial one in both scenarios. Below a critical λ_c , Figs. 7(a) and 7(d) display a prominent set of edge states traversing from CB to VB through FB (and vice versa) for $\alpha = 0.1$ and 0.2 , respectively

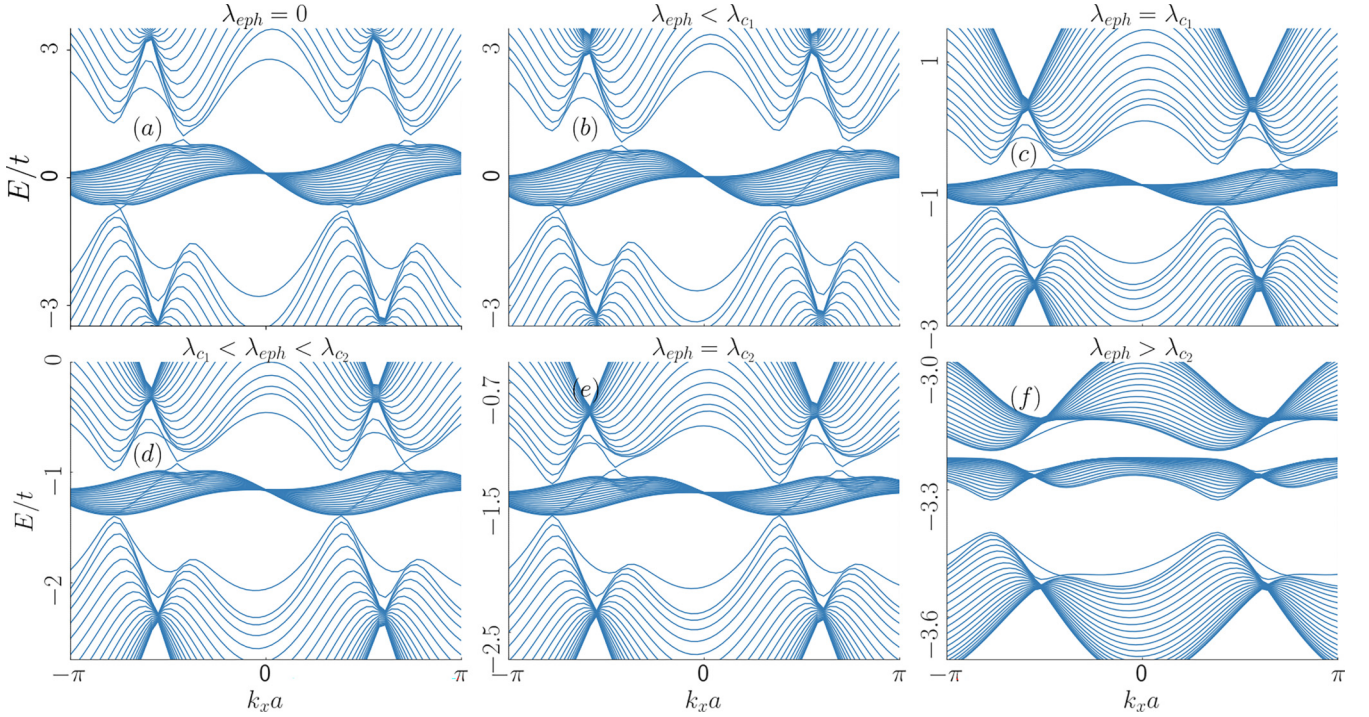


FIG. 8. Energy spectra (in units of t) of the edge states are shown for a zigzag edged semi-infinite ribbon as a function of dimensionless momenta, k_x (multiplied by the lattice constant) of $\alpha = 0.7$ for (a) $\lambda_{\text{eph}} = 0$, (b) $\lambda_{\text{eph}} = 0.2$ ($\lambda_{\text{eph}} < \lambda_{c_1}$), (c) $\lambda_{\text{eph}} = \lambda_{c_1} = 0.28$, (d) $\lambda_{\text{eph}} = 0.35$ ($\lambda_{c_1} < \lambda_{\text{eph}} < \lambda_{c_2}$), (e) $\lambda_{\text{eph}} = \lambda_{c_2} = 0.43$, and (f) $\lambda_{\text{eph}} = 0.6$ ($\lambda_{\text{eph}} > \lambda_{c_2}$). Other parameters are the same as those in Fig. 5. The values of λ_{c_1} and λ_{c_2} are mentioned in Table II.

for the $\lambda_{\text{eph}} < \lambda_c$ regime. We notice that a pair of edge states emerge from different valleys in the bulk, gather at the FBs and hence cross over to the CBs. By looking at the slope of the edge states, that is, $\partial E / \partial k$, which is a measure of the velocity of the electron, we infer that the flow of the edge currents is counterpropagating, as it should be. These edge states are the chiral edge states of a Chern insulator, appearing in the regime of $\lambda_{\text{eph}} < \lambda_c$. The nature of the edge states for the $\alpha = 0.2$ case are distinct, in the sense that they are crossing the FB at different points. It is also visible in Figs. 7(b) and 7(e) that these chiral edges persist up to $\lambda_{\text{eph}} = \lambda_c$ and disappear beyond that. These are presented in Figs. 7(c) and 7(f), that for values above λ_c , the edge states completely disappear and bulk spectra become gapped, signifying the transition of the system to a trivial phase. The critical values of λ_{eph} corresponding to the transitions for the $\alpha = 0.1$ and $\alpha = 0.2$ cases are listed in Table I. Therefore, in α - T_3 systems (with smaller α values), one can generate topological insulating phases via only tuning λ_{eph} for a particular value of α below a certain λ_c , beyond which the system goes into a trivial insulating phase. Next, let us study the characteristics of the edge states for higher α values, and as a specific case, consider $\alpha = 0.7$, presented in Fig. 8. In reference to its bulk properties displayed in Fig. 5, we shall examine the edge states for different regimes of λ_{eph} . As discussed in Figs. 5(a) and 5(b), the bulk FB and VB remain in contact with each other for the $\lambda_{\text{eph}} \lesssim \lambda_{c_1}$ region, we notice its signature in Figs. 8(a) and 8(b), where a pair of counterpropagating edge states emerge near each K valley, passing through the FB for the $\lambda_{\text{eph}} \lesssim \lambda_{c_1}$ regime. However, in this regime of λ_{eph} , the notion of edge states is not important as the system does not have any bulk gap, inferring it to be a

usual semimetal. The edge states connecting the VB and CB through the FB are gapped till $\lambda_{\text{eph}} = \lambda_{c_1}$ at which the edge states at one K -valley touch for the first time [can be seen clearly if we zoom in Fig. 8(c)], thereby generating a conducting edge mode. In the intermediate region [see Fig. 8(d)], i.e., for $\lambda_{c_1} < \lambda_{\text{eph}} < \lambda_{c_2}$, the system clearly exhibits the presence of edge states indicating a topologically nontrivial (Chern insulating) phase. It is evident in Fig. 8(d) that the edge states are counterpropagating, and they cross the FB at the two edges for $\lambda_{c_1} < \lambda_{\text{eph}} < \lambda_{c_2}$. Therefore, for $\alpha = 0.7$, there seems to be a re-entrant mechanism to the SM phase, which may be achieved entirely by tuning the e-ph coupling strength. Around $\lambda_{\text{eph}} = \lambda_{c_2}$, the edge states start fading out [shown in Fig. 8(e)] at one K valley and is completely disappear above λ_{c_2} [see Fig. 8(f)]. Undoubtedly, the $\lambda_{\text{eph}} > \lambda_{c_2}$ region refers to a trivial insulator with no sign of edge states. As suggested in the discussion of the bulk spectra (Sec. III A) that multiple phase transitions (insulator-SM-insulator-SM-insulator) can occur for $\alpha > 0.7$, we explicitly plot the edge states for $\alpha = 0.8$ in Fig. 9 which ascertains whether the insulating phases are topological. In Fig. 9(a), we notice that in the absence of e-ph coupling, a pair of prominent edge states cross the FB at K or K' valley, signifying a topologically nontrivial Chern insulating phase (unlike for $\alpha = 0.7$ where it is SM), which remain intact in the $\lambda_{\text{eph}} < \lambda_{c_1}$ regime [Fig. 9(b)] till $\lambda_{\text{eph}} = \lambda_{c_1}$. At this value one pair of edge states becomes gapped at one valley, while in the other valley it remains gapless [Fig. 9(c)]. However, such as for the $\alpha > 0.7$ case, it is vividly seen in Figs. 9(d)–9(f) that the counterpropagating edge states resurface in the $\lambda_{c_1} < \lambda_{\text{eph}} < \lambda_{c_2}$ regime, persist up to $\lambda_{\text{eph}} = \lambda_{c_2}$ and completely vanish beyond λ_{c_2} . So, for

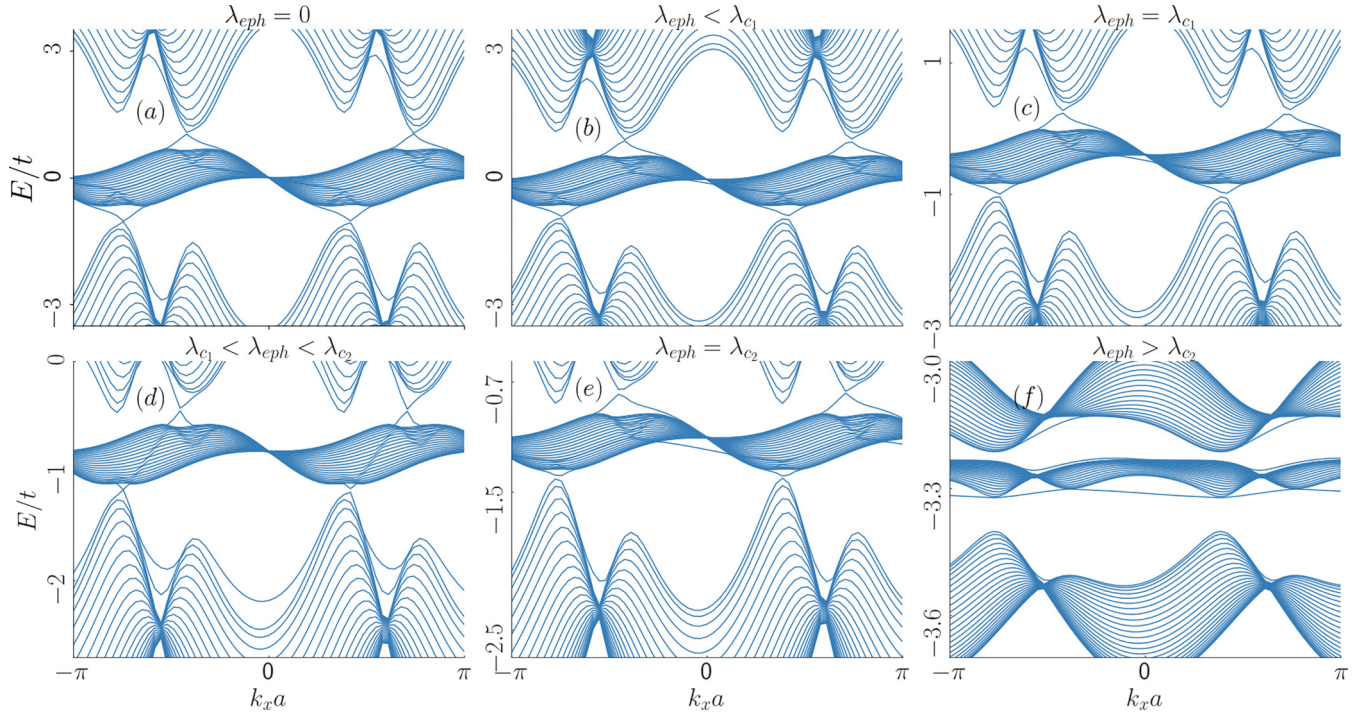


FIG. 9. Energy spectra (in units of t) of the edge states are shown for a zigzag edged semi-infinite ribbon as a function of dimensionless momenta, k_x (multiplied by the lattice constant) of $\alpha = 0.8$ for (a) $\lambda_{\text{eph}} = 0$, (b) $\lambda_{\text{eph}} = 0.15$ ($\lambda_{\text{eph}} < \lambda_{c_1}$), (c) $\lambda_{\text{eph}} = \lambda_{c_1} = 0.2$, (d) $\lambda_{\text{eph}} = 0.35$ ($\lambda_{c_1} < \lambda_{\text{eph}} < \lambda_{c_2}$), (e) $\lambda_{\text{eph}} = \lambda_{c_2} = 0.44$, and (f) $\lambda_{\text{eph}} = 0.6$ ($\lambda_{\text{eph}} > \lambda_{c_2}$). Other parameters are the same as those in Fig. 6. The values of λ_{c_1} and λ_{c_2} are mentioned in Table II.

$\alpha = 0.8$ as well, the re-entrant scenario to the SM phase still holds (also true for $\alpha = 0.9$, not shown here). To confirm that the edge modes indeed correspond to a Chern insulating phase, we compute the topological properties and discuss them for each of the regions of λ_{eph} (as indicated above) in the following section (Sec. III C). The phase transition points, namely λ_{c_1} and λ_{c_2} for $\alpha = 0.7, 0.8$, and 0.9 are listed in Table II.

C. Berry curvature and Chern number

To ascertain the topological signatures in the α - T_3 induced by the e-ph coupling, we numerically compute the topological ingredients, namely, the (polaronic) Berry curvature and the Chern number. We also obtain the phase diagram containing the Chern number and e-ph coupling strength. In a usual α - T_3 lattice, due to the TRS breaking NNN Haldane term, the system exhibits a nonzero Chern number. The onsite Samenoff mass term that breaks the valley degeneracy also plays a crucial role in band opening at high symmetry Dirac points. However, our main aim is to investigate how e-ph interaction mediates a nonzero Chern number in the system for a fixed set of other system parameters, namely, λ and M . We expect that there should exist an interplay between the mass term and the e-ph coupling. Therefore we may achieve a topological transition only by tuning the strength of e-ph coupling, λ_{eph} .

The Chern number (C) can be calculated as

$$C = \frac{1}{2\pi} \iint_{\text{BZ}} \Omega(k_x, k_y) dk_x dk_y, \quad (14)$$

where $\Omega(k_x, k_y)$ is the Berry curvature of our system expressed as

$$\Omega(k_x, k_y) = -2i \Im \left[\left\langle \frac{\partial \psi(k_x, k_y)}{\partial k_x} \middle| \frac{\partial \psi(k_x, k_y)}{\partial k_y} \right\rangle \right], \quad (15)$$

where $\psi(k_x, k_y)$ refers to the eigenstate of the modified Haldane model, which is the polaronic bulk band and \Im denotes the imaginary part. The topological phase transition is characterized by a topological invariant. In our study, it is the (polaronic) Chern number, C , displayed in Eq. (14). In order to calculate so, we first compute the Berry curvature, $\Omega(k_x, k_y)$ using Eq. (15) corresponding to the VB and integrate it over the entire BZ. We plot $\Omega(k_x, k_y)$ in Figs. 10–12 and C in Fig. 14 to investigate the topological phase transition explicitly mediated through the e-ph coupling.

In Fig. 10, we show the Berry curvatures in three different regions of λ_{eph} i.e., $\lambda_{\text{eph}} < \lambda_c$, $\lambda_{\text{eph}} \sim \lambda_c$ (“ \sim ” sign refers to values close to it, but not at it), and $\lambda_{\text{eph}} > \lambda_c$ in left, middle and right panels, respectively for smaller values of α , namely, $\alpha = 0.1, 0.2$, and 0.3 (marked on the right edge). It is generally true that a nonzero Berry curvature is a direct consequence of a nontrivial topology present in the system. The corresponding values seen to be concentrated at the high symmetry points K and K' . However, the change in the concentration of the Berry curvatures shown by colormaps in Figs. 10–12 sets the precursor for any topological transition happening in the system. For $\alpha = 0.1$ [Fig. 10(a)], we clearly observe that below the critical λ_c (i.e., $\lambda_{\text{eph}} < \lambda_c$ regime) the Berry curvatures are equally distributed in the six corners of the hexagon which defines a topologically

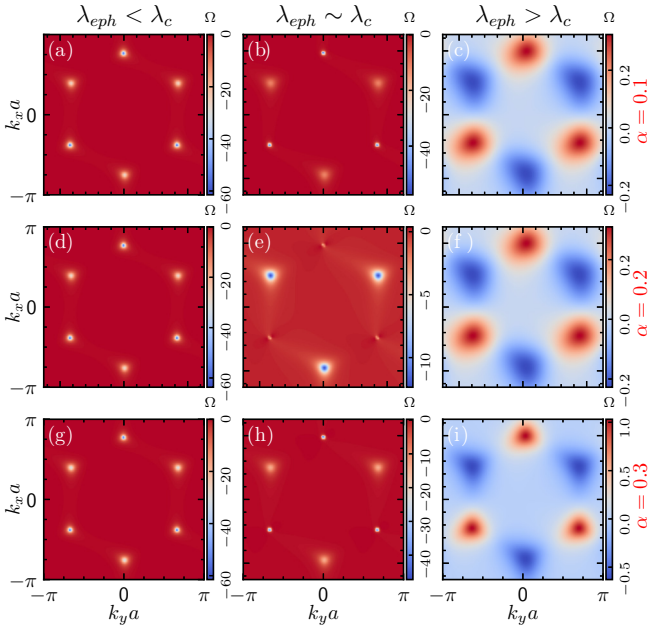


FIG. 10. The Berry curvature corresponding to the VB is presented for lower α -values in different regimes of λ_{eph} . (Left column) Those are plotted in the $\lambda_{\text{eph}} < \lambda_c$ regime for (a) $\alpha = 0.1$, (d) 0.2, and (g) 0.3, at $\lambda_{\text{eph}} = 0.3$. (Middle column) At the critical $\lambda_{\text{eph}} (= \lambda_c)$ for (b) $\alpha = 0.1$, $\lambda_c = 0.49$; (e) $\alpha = 0.2$, $\lambda_c = 0.48$; and (h) $\alpha = 0.3$, $\lambda_c = 0.47$. (Right column) The same are shown in the $\lambda_{\text{eph}} > \lambda_c$ regime for (c) $\alpha = 0.1$, (f) 0.2, and (i) 0.3, at $\lambda_{\text{eph}} = 0.6$. Other parameters are mentioned in Fig. 3. The values of λ_c are mentioned in Table I.

nontrivial phase with a nonzero Chern number. However, as λ_{eph} is increased, the concentration changes. As the Berry curvature is singular at the critical point, we plot it in the vicinity of the critical point ($\lambda_{\text{eph}} \sim \lambda_c$) shown in Fig. 10(b). Interestingly, as λ_{eph} approaches λ_c , we notice a clear distinction in the concentration of the Berry curvatures at K and K'

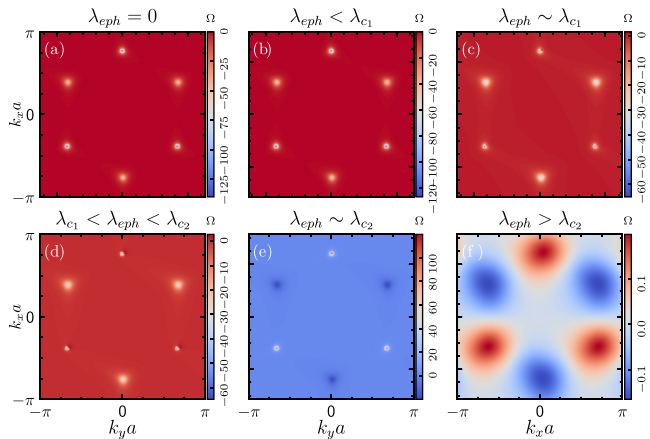


FIG. 11. The Berry curvature corresponding to the VB is presented for $\alpha = 0.7$ in different regimes of λ_{eph} for (a) $\lambda_{\text{eph}} = 0$, (b) $\lambda_{\text{eph}} < \lambda_{c1}$ ($\lambda_{\text{eph}} = 0.2$), (c) $\lambda_{\text{eph}} \sim \lambda_{c1}$ ($\lambda_{\text{eph}} = 0.26$), (d) $\lambda_{c1} < \lambda_{\text{eph}} < \lambda_{c2}$ ($\lambda_{\text{eph}} = 0.35$), (e) $\lambda_{\text{eph}} \sim \lambda_{c2}$ ($\lambda_{\text{eph}} = 0.41$), and (f) $\lambda_{\text{eph}} > \lambda_{c2}$ ($\lambda_{\text{eph}} = 0.6$). Other parameters are mentioned in Fig. 5. The values of λ_{c1} and λ_{c2} are mentioned in Table II.

points. At the K point, the concentrations are predominantly higher compared to those at the K' point. This observation can also be explained via Fig. 3(b) where at $\lambda_{\text{eph}} = \lambda_c$, we see a sharp mismatch in the behavior of the bulk bands at K and K' points, where at one K point, the FB and VB touch each other, while they remain gapped at the K' point, displaying the contrasting effects of the e-ph coupling on the FB at two valleys. For other α values ($\alpha = 0.2$ and $\alpha = 0.3$) that are plotted in Figs. 10(e) and 10(h), the distinction between the Berry curvatures at K and K' points is much more prominent. In Fig. 10(c), we show that the Berry curvatures above the critical e-ph coupling strength are almost equal and opposite at K and K' points thereby canceling each other resulting in a topologically trivial phase with a zero Chern number. Hence, till the critical λ_c , the system remains in the topologically nontrivial phase exhibiting a nonzero Chern number. We wish to mention that we have also observed almost similar variations of the Berry curvature by varying the e-ph coupling for the intermediate range of α , namely, $\alpha = 0.4, 0.5$, and 0.6 (not shown here).

To show the variations of the Berry curvature of $\alpha = 0.7$, we plot Fig. 11 that can be explained with the help of the bulk and edge spectra displayed in Figs. 5 and 8, respectively. Let us first look at Figs. 11(a) and 11(b), which is for $\lambda_{\text{eph}} = 0$ and $\lambda_{\text{eph}} < \lambda_{c1}$, respectively. In this regime, as we have discussed, the spectral gap between the FB and VB vanishes even at $\lambda_{\text{eph}} = 0$, and remains so till $\lambda_{\text{eph}} = \lambda_{c1}$, manifesting the chiral edge states [see Figs. 8(a) and 8(b)] at the boundaries. However, in this regime, the Berry curvature shows singular behavior as there is no bulk gap, and consequently, the Chern number is ill-defined. However, as we tune λ_{eph} further, a bulk gap opens up for the first time at around $\lambda_{\text{eph}} \sim \lambda_{c1}$ [see Fig. 5(c)], where we see that the concentrations at the K points start behaving differently than that at K' points and are shown in Fig. 11(c). Beyond λ_{c1} , this signature is much more noticeable [can be seen in Fig. 11(d)] and the edge states are prominent [see Fig. 8(d)] in $\lambda_{c1} < \lambda_{\text{eph}} < \lambda_{c2}$ regime. In the vicinity of $\lambda_{\text{eph}} = \lambda_{c2}$, the bulk gap closes showing high values for the Berry curvature [see Fig. 11(e)]. Finally beyond λ_{c2} [Fig. 11(f)], the variation of the Berry curvature is reminiscent of Figs. 10(c), 10(f), and 11(i) enunciates the onset of a trivial insulating phase.

The Berry curvature plots for $\alpha = 0.8$ are displayed in Fig. 12. Although the variations in the $\lambda_{\text{eph}} < \lambda_{c1}$ regime (Fig. 12(b)) may look similar to those for $\alpha = 0.7$ showing higher values of the Berry curvatures even for $\lambda_{\text{eph}} = 0$ [Fig. 12(a)], but with the support of the findings of Figs. 6 and 9 described in Sec. III A and III B respectively, it is ensured that in the $0 \leq \lambda_{\text{eph}} < \lambda_{c1}$ regime, they may correspond to some topological phase (unlike the usual SM phase for $\alpha = 0.7$) with conducting edge modes [see Figs. 9(a) and 9(b)] associated with higher Chern numbers. The observations of Figs. 12(c)–12(f) are almost same as $\alpha = 0.7$ case. However, a noticeable dissimilarity with the $\alpha = 0.7$ variation in the Berry curvature can be observed for the $\lambda_{c1} < \lambda_{\text{eph}} < \lambda_{c2}$ regime [Fig. 12(d)], where the disparity between the concentrations of the Berry curvature at two valleys is much more significant compared to that for $\alpha = 0.7$. This makes the variation of Fig. 12(d) distinguishable from Figs. 12(a) and 12(b) denoting different topological phases.

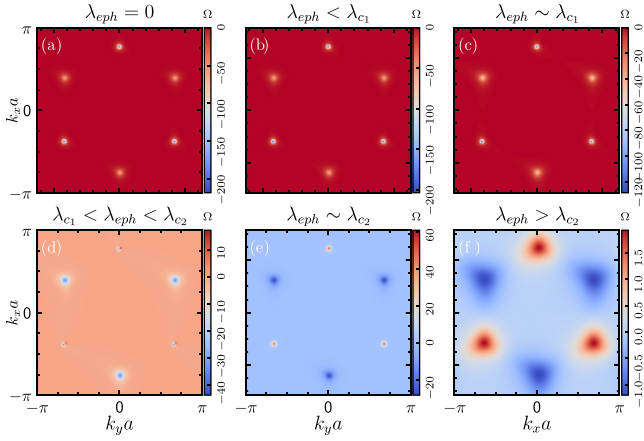


FIG. 12. The Berry curvature corresponding to the VB is presented for $\alpha = 0.8$ in different regimes of λ_{eph} for (a) $\lambda_{\text{eph}} = 0$, (b) $\lambda_{\text{eph}} < \lambda_{c_1}$ ($\lambda_{\text{eph}} = 0.15$), (c) $\lambda_{\text{eph}} \sim \lambda_{c_1}$ ($\lambda_{\text{eph}} = 0.18$), (d) $\lambda_{c_1} < \lambda_{\text{eph}} < \lambda_{c_2}$ ($\lambda_{\text{eph}} = 0.35$), (e) $\lambda_{\text{eph}} \sim \lambda_{c_2}$ ($\lambda_{\text{eph}} = 0.42$), and (f) $\lambda_{\text{eph}} > \lambda_{c_2}$ ($\lambda_{\text{eph}} = 0.6$). Other parameters are mentioned in Fig. 6. The values of λ_{c_1} and λ_{c_2} are mentioned in Table II.

To confirm the topological phase transition induced by the polaronic interaction in the system, we numerically compute the Chern number C using Eq. (14) and examine the variation with the e-ph coupling strength λ_{eph} .

However, before going into the intricacies of the electron-phonon interaction, let us take a moment to briefly examine the topological phase transition of the bare Haldane α - T_3 lattice. In Fig. 13, we illustrate how a Haldane term on an α - T_3 lattice renders the system a Chern insulating phase that is characterized by a nonzero Chern number. Tuning the parameter α , a topological phase transition occurs at $\alpha = 0.5$. This transition alters the Chern number of the VB (CB) from $C = -1(1)$ to a larger Chern number, $C = -2(2)$. These findings precisely align with previously reported results regarding topological phase transitions in α - T_3 lattices [49].

Now let us examine the dependency of the Chern number on α in the presence of the e-ph interaction. Figure 14 displays

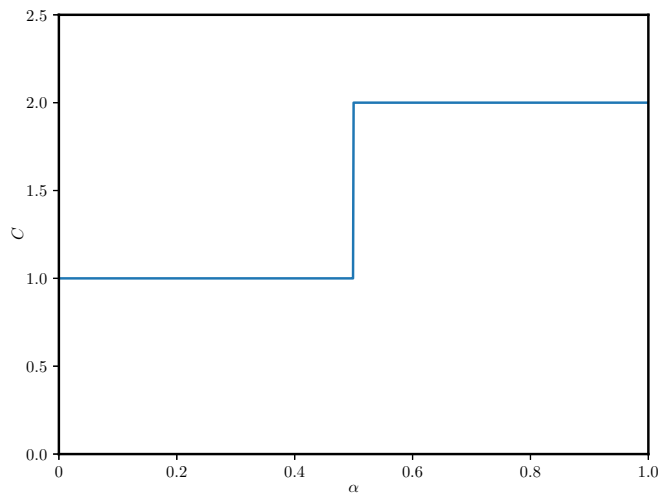


FIG. 13. Chern number, C as a function of α for the bare (without e-ph coupling and mass term) Haldane model of an α - T_3 lattice.

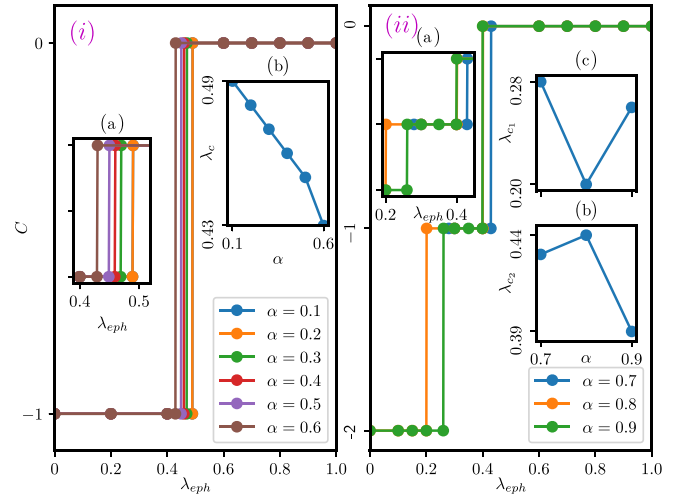


FIG. 14. The Chern number C corresponding to the VB as a function of e-ph coupling strength λ_{eph} for (i) lower to intermediate α values ($0 < \alpha \leq 0.6$) is shown, while in inset (a) a zoomed in picture of the transition regions, and in the inset (b), the variation of λ_c as a function of α is shown. In (ii), the variations of C for larger α values ($0.6 < \alpha \leq 0.9$) are shown. Inset (a) represents a zoomed in picture of the transition regions, while insets (b) and (c), respectively, display the variations of λ_{c_2} and λ_{c_1} as a function of α . The values of λ_c are mentioned in Tables I and II.

the variations of the Chern number as a function of λ_{eph} . Here, we display the variations of C separately in two diagrams for lower to intermediate values of α ($\alpha = 0.1, 0.2, \dots, 0.6$) [see Fig. 14(i)] and larger values of α ($\alpha = 0.7, 0.8, 0.9$) [see Fig. 14(ii)]. Starting from the $\alpha = 0.1$ case to the intermediate values, such as $\alpha = 0.6$, we notice that $C = -1$ up to a critical λ_c , at which C abruptly falls to $C = 0$ showing a sharp discontinuity. Therefore, for lower to intermediate cases of α [Fig. 14(i)], the system initially behaves like a Chern insulator designated by a nonzero Chern number until the e-ph coupling reaches a certain critical value, λ_c (λ_c 's are listed in Table I) at which the system undergoes a topological transition accompanied by the closing of the bulk gap and emerging signatures of the edge states. While, beyond λ_c , the system ceases to host edge states which is a typical signature of a trivial insulator for which $C = 0$. We display a zoomed in picture of the transition points in the inset (a) of Figs. 14(i) and 14(ii). In inset (b) of Fig. 14(i), we depict the variation of the critical λ_c with respect to α , illustrating a nearly linear decrease with increasing α .

It is understood by now that such variations at higher α values are in contrast to those at lower values of α . Let us first consider the variation corresponding to $\alpha = 0.7$ which is represented via a solid blue line in Fig. 14(ii). Unlike the lower α values, there exist two transition points, namely, λ_{c_1} and λ_{c_2} for higher α values (listed in Table II). Below the former, the system inherits a conventional SM phase (where C is ill-defined), and above the latter, the system becomes a trivial insulator. Understandably, the $\lambda_{c_1} < \lambda_{\text{eph}} < \lambda_{c_2}$ region is our main interest for $\alpha = 0.7$, where we find that the Chern number is fixed at $C = -1$ that underscores the emergence of a topologically nontrivial insulating phase, driven

entirely by the e-ph coupling. As expected, beyond λ_{c_2} , C becomes zero confirming the onset of a trivial phase. Thus the e-ph coupling favors a transition from a semi-metal to a topological insulator, and to a trivial insulator for $\alpha = 0.7$. However, the $0 \leq \lambda_{\text{eph}} < \lambda_{c_1}$ regime becomes interesting for $\alpha > 0.7$ as described earlier in the findings of Figs. 9(a) and 9(b) that the conducting edge modes exist (specifically for $0.8 \leq \alpha < 1$) in that regime of λ_{eph} indicating a topologically nontrivial insulating phase. In Fig. 14(ii), we plot C as a function of λ_{eph} for $\alpha = 0.8$ denoted by the solid orange line, where higher Chern number, namely $C = -2$ in $0 \leq \lambda_{\text{eph}} < \lambda_{c_1}$ regime is noted, confirming emergence of a distinct (other than $C = -1$) topological phase. Nevertheless, as we tune λ_{eph} further, the scenario becomes exactly the same as $\alpha = 0.7$, that is, C changes from $C = -2$ to -1 at $\lambda_{\text{eph}} = \lambda_{c_1}$ signifying a different topological phase that persists in the $\lambda_{c_1} < \lambda_{\text{eph}} < \lambda_{c_2}$ regime, which finally vanishes beyond λ_{c_2} . A similar observation is also shown for $\alpha = 0.9$ (marked by the solid green line). Therefore, for the $0.7 < \alpha < 1$ regime, the system undergoes a transition from one topological phase ($C = -2$) to another ($C = -1$) and hence transits to a trivial ($C = 0$) phase, purely mediated all the while by the e-ph coupling. The emergence of $|C| = 2$ topological phase in an α - T_3 is a familiar phenomenon obtained by others [43,49,72] in the absence of e-ph interaction. For our case, the results completely match with those in Ref. [49] corresponding to $\lambda_{\text{eph}} \rightarrow 0$ and $M \rightarrow 0$ (shown in Fig. 13). Moreover, due to the e-ph interaction, we obtain a $|C| = 2$ topological phase for lower values of λ_{eph} , even at $\lambda_{\text{eph}} = 0$ (in $0 \leq \lambda_{\text{eph}} < \lambda_{c_1}$ regime) for $0.8 \leq \alpha < 1$, that is for α values close to the dice lattice limit ($\alpha = 1$). As earlier, in insets (b) and (c) of Fig. 14(ii), we show the variation of the critical λ_{c_2} and λ_{c_1} , respectively as a function of α . We observe that λ_{c_1} initially decreases and then increases with increasing α , whereas an opposite trend is observed for λ_{c_2} , namely, it increases first and hence decreases with increasing α . We should mention that the findings of Chern number plots are completely consistent with those of bulk and edge spectra for different regimes of λ_{eph} . As stated in Sec. III A, although we have shown a few cases of α , it is also important to note that this kind of transition can occur for any value of α ($0 < \alpha < 1$). Therefore it seems robust that the polaron formation in α - T_3 lattices induces a topological phase transition generated solely due to the presence of e-ph coupling.

So far we have discussed the topological transitions for different α - T_3 lattices taking discrete values of α in the range $[0 : 1]$. A phase diagram is hence computed in the $\lambda_{\text{eph}} - \alpha$ plane to show the exact locations of different (topological/SM/trivial) phases in the parameter space. The phase diagram containing the Chern number (C) corresponding to the VB, in the parameter space defined by e-ph interaction (λ_{eph}) and α for fixed values of λ and M , is depicted in Fig. 15. It is evident that the teal area represents a topological phase of the system with a Chern number as $C = -1$ in the $\lambda_{\text{eph}} < \lambda_c$ regime for $0 < \alpha \lesssim 0.65$ and in the $\lambda_{c_1} \leq \lambda_{\text{eph}} \leq \lambda_{c_2}$ regime for $0.65 \lesssim \alpha < 1$. Furthermore, for $0.65 \lesssim \alpha \lesssim 0.75$ regime, there exists an SM region (where C is ill-defined due to the closing of the bulk band gap) denoted by the grey color corresponding to λ_{eph} values in the $0 \leq \lambda_{\text{eph}} \leq \lambda_{c_1}$ regime, signifying that the system behaves like a

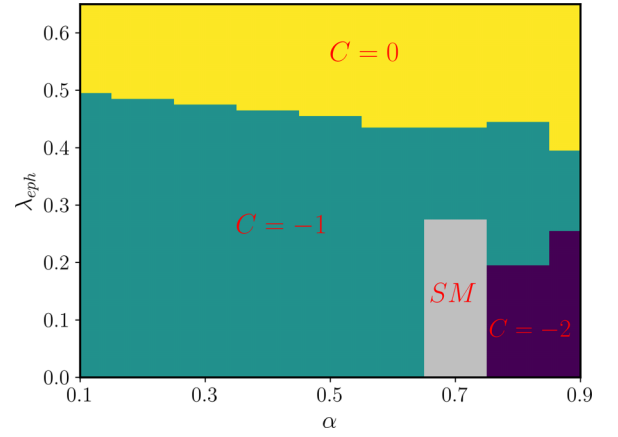


FIG. 15. The topological phase diagram based on the Chern number (C) corresponding to the VB in the $\lambda_{\text{eph}} - \alpha$ plane. The nonzero C corresponding to the teal region is denoted as $C = -1$, while the yellow region represents the vanishing Chern number ($C = 0$), signifying a (topologically trivial) CDW phase. The grey region denotes the SM phase for $0.65 \lesssim \alpha \lesssim 0.75$, while the deep purple region stands for a distinct topological phase with $C = -2$ for $0.75 \lesssim \alpha < 1$. Other parameters remain the same as mentioned in Fig. 3.

conventional semimetal. While in the same regime of λ_{eph} , an α - T_3 lattice with $0.75 \lesssim \alpha < 1$ exhibits a distinct topological phase with $C = -2$ (the deep purple region). The yellow region denotes a trivial phase with $C = 0$ for all values of α ($0 < \alpha < 1$) above their respective critical λ_c points (listed in Tables I and II). It may be noted that varying the parameters λ and M can significantly alter the phase diagram. However, we do not show them here for brevity. Let us explore the possibility of charge ordering in our system. In a 2D tight-binding Holstein model, a charge density wave (CDW) ordered state is an intriguing phenomenon [105–113]. In our case, due to the presence of e-ph interaction, the electrons interact with the dispersionless (optical) phonons, and as a result, the lattice gets distorted, giving rise to polarons, which may drive the system towards the formation of a CDW state. The direct consequence of e-ph interaction in our system can be understood mathematically from Eq. (7), where the hopping terms (t and λ) are renormalized by the Holstein factor, plus an additional term is added to the onsite energy as the polaron shift energy ($-\lambda_{\text{eph}}^2 \hbar \omega_0$) that further lowers the energy of the system. In the high e-ph coupling ($\lambda_{\text{eph}} \gg t, \lambda$) regime, these effects dominate over those due to the other parameters of the system, and may eventually favor the formation of the CDW ordered state. To confirm the existence of the charge ordering in our system, we proceed as follows. The density in the momentum space can be expressed as $\rho(\mathbf{k}) = \sum_i e^{-i\mathbf{k}\cdot\mathbf{r}_i} \langle n_i \rangle$, where $\langle n_i \rangle$ is the expectation value of the electron density operator with respect to the ground state of the system for the i th site, with \mathbf{k} and \mathbf{r}_i denoting the wave vector and the real space lattice vector, respectively. As our system comprises of three sublattices, namely, A , B , and C , we numerically calculate $\rho(\mathbf{k})$ for the individual sublattice in the momentum space and symbolize them as ρ_A , ρ_B , and ρ_C corresponding to the A , B , and C sites, respectively. We further show the variations

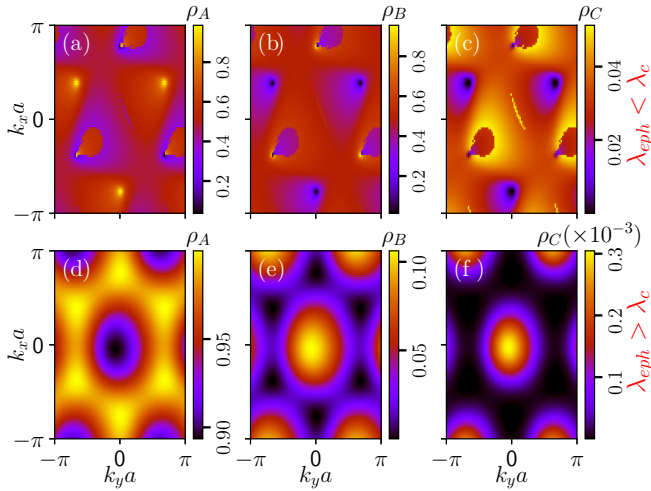


FIG. 16. For $\alpha = 0.3$: the contour plots of the CDW order parameter, ρ corresponding to individual sites, namely ρ_A , ρ_B and ρ_C for A , B , and C sites, respectively are plotted in the k_x - k_y plane. (a)–(c) (top panel) display those in the $\lambda_{\text{eph}} < \lambda_c$ ($\lambda_{\text{eph}} = 0.1$) regime, while (d)–(f) (bottom panel) display the same for the $\lambda_{\text{eph}} > \lambda_c$ ($\lambda_{\text{eph}} = 0.6$) regime, $\lambda_c = 0.47$ for $\alpha = 0.3$. The parameters are the same as mentioned in Fig. 3.

of ρ_A , ρ_B and ρ_C in the k_x - k_y plane (Fig. 16) in the form of a contour plot for low ($\lambda_{\text{eph}} < \lambda_c$) and high ($\lambda_{\text{eph}} > \lambda_c$) e-ph coupling regimes to investigate the distribution of the electron densities at these individual lattice sites as a function of the e-ph coupling strength. The plot displays the variation of the densities, ρ_A , ρ_B , and ρ_C for $\alpha = 0.3$. The low and high e-ph coupling regimes are designated as $\lambda_{\text{eph}} < \lambda_c$ (top panel) and $\lambda_{\text{eph}} > \lambda_c$ (bottom panel), respectively, where λ_c denotes the (topological) transition point. In Figs. 16(a) and 16(b), one may notice that electron densities ρ_A and ρ_B are distributed almost equally for A and B sublattices when the e-ph coupling is small ($\lambda_{\text{eph}} < \lambda_c$). The density at the C site, namely, ρ_C [Fig. 16(c)] is not significant here, which makes sense as the hopping amplitude between A and C (αt) sites is small ($\alpha = 0.3$). However, with the densities at A and B being equal, any charge ordering appears to be absent. Interestingly, for the high e-ph coupling regime ($\lambda_{\text{eph}} > \lambda_c$), we observe an interesting feature as displayed in Figs. 16(d)–16(f). It shows that the electron density for the A sublattice [ρ_A in Fig. 16(d)] is distributed almost in the entire \mathbf{k} space, while the contributions of the B [ρ_B in Fig. 16(e)] and C [ρ_C Fig. 16(f)] sites are minimal. The prominent instability of the electron densities should result in a significantly high (spanning almost the entire BZ) concentration only at the A -site in the $\lambda_{\text{eph}} > \lambda_c$ regime, indicating a charge ordered state.

A better visualization of the modulation of the charge order in the momentum space can be achieved if we plot the variations of ρ_A , ρ_B , and ρ_C along a particular direction in k -space, namely, k_x , while keeping $k_y = 0$ in $\lambda_{\text{eph}} < \lambda_c$ [Figs. 17(a)–17(c) in the left panel] and $\lambda_{\text{eph}} > \lambda_c$ [Figs. 17(d)–17(f) in the right panel] regimes. It can be clearly observed from Figs. 17(a)–17(c) that ρ_A and ρ_B exhibit peaks with their extrema of almost equal magnitudes and occurring at the same k_x values, while those for ρ_C being negligibly small [can

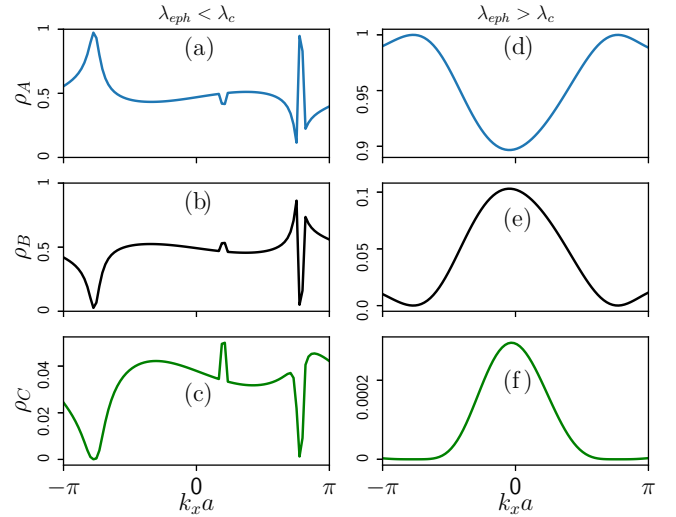


FIG. 17. For $\alpha = 0.3$: the modulation of CDW order parameter as a function of dimensionless momenta, k_x (multiplied by the lattice constant) is shown at $k_y = 0$. (a)–(c) (left panel) respectively represent the modulation of ρ_A (blue), ρ_B (black), and ρ_C (green) in the $\lambda_{\text{eph}} < \lambda_c$ regime, while (d)–(f) (right panel) display the same for the $\lambda_{\text{eph}} > \lambda_c$ regime. All the parameters are kept the same as those in Fig. 3.

also be understood from Figs. 16(a)–16(c)] for the $\lambda_{\text{eph}} < \lambda_c$ regime. However, these peaks are not periodically modulated over the BZ and thus there is no evidence of charge ordering in the $\lambda_{\text{eph}} < \lambda_c$ regime. Interestingly, for $\lambda_{\text{eph}} > \lambda_c$, the electron density is not only concentrated entirely at the A sublattice at a particular value of k_x where it shows a high peak (ρ_B and ρ_C being negligibly small), it also modulates periodically as a function of k_x [Fig. 17(d)]. Along with, we observe the periodic modulations in ρ_B [Fig. 17(e)] and ρ_C [Fig. 17(f)] (albeit much weaker), which elucidates formation of a CDW ordered state. It is important to mention that the variations of the density for other α value in range $[0 : 1]$ are similar to those in Figs. 16 and 17, with the density of C sublattice scaling with α values. Thus our system facilitates a CDW ordered phase only in the high e-ph coupling ($\lambda_{\text{eph}} > \lambda_c$) regime.

As in our study, the system displays topological signatures in the lower e-ph coupling regime ($\lambda_{\text{eph}} < \lambda_c$), and not at higher values of λ_{eph} , we therefore, infer that the charge ordered phase is present only in the trivial regime and a coexistence of charge order and topology does not occur in our system. Hence, in the phase diagram (Fig. 15), the trivial insulating phase marked by the yellow region (designated as $C = 0$) hosts a CDW ordered phase, while the teal ($C = -1$) and the deep purple ($C = -2$) regions do not demonstrate any charge ordering.

D. Hall conductivity

In this section, we numerically compute the polaronic Hall conductivity using the following expression:

$$\sigma_{xy} = \frac{e^2}{2\pi h} \sum_{\gamma} \int \frac{dk_x dk_y}{4\pi^2} f(E_{k_x, k_y}^{\gamma}) \Omega(k_x, k_y), \quad (16)$$

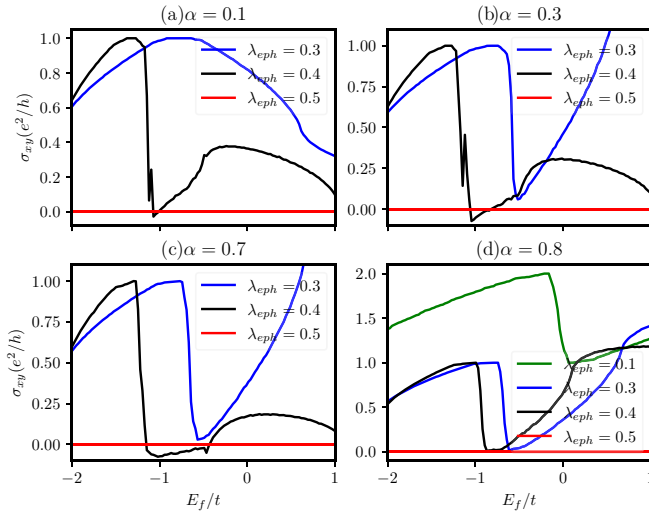


FIG. 18. The Hall conductivity, σ_{xy} , as a function of Fermi energy, E_f is presented for various values of α : (a) $\alpha = 0.1$, (b) 0.3 , (c) 0.7 , and (d) 0.8 for different λ_{eph} values that are shown in the inset. Other parameters are the same as mentioned in Fig. 3.

where $e^2/h = \sigma_0$ is the scale in which σ_{xy} is measured, E_{k_x, k_y}^γ is the energy band with the band index $\gamma = -1, 0$, and $+1$ corresponding to the VB, FB, and CB, respectively, f denotes the Fermi-Dirac distribution function: $f(E) = [1 + e^{(E-E_F)/k_B T}]^{-1}$, E_F and T being the Fermi energy and the absolute temperature, respectively, $\Omega(k_x, k_y)$ being the Berry curvature. Figure 18 display the variations of the polaronic Hall conductivities at $T = 0$ as a function of E_f for different values of e-ph interaction strength, λ_{eph} for $\alpha = 0.1$ [see Fig. 18(a)], $\alpha = 0.3$ [Fig. 18(b)], $\alpha = 0.7$ [Fig. 18(c)], and $\alpha = 0.8$ [Fig. 18(d)].

As shown in Fig. 18(a), the Hall conductivity (σ_{xy}) is plotted as a function of the Fermi energy (E_f) for $\lambda_{\text{eph}} = 0.3, 0.4$, and 0.5 marked by solid blue, black and red colors, respectively. It is observed for $\alpha = 0.1$, the Hall conductivities initially increase and show tiny plateaus [can also be seen in Figs. 18(b) and Fig. 18(c) for $\alpha = 0.3$ and 0.7 , respectively], which are quantized at a value e^2/h for the $\lambda_{\text{eph}} < \lambda_c$ regime. In other words, these quantized plateaus occurring at $|C|e^2/h$ (here, $|C| = 1$) presented in Fig. 18(a) reconfirm that up to a critical e-ph coupling $\lambda_c = 0.49$, the system behaves like a topological insulator. Beyond the critical λ_c (denoted by solid red), it becomes a trivial insulator with $\sigma_{xy} = 0$ (that is, $C = 0$). Similar observation is noted in Fig. 18(c) for $\alpha = 0.7$ where the plateaus at values $|C|e^2/h$ exist for λ_{eph} values that are in the $\lambda_{c1} < \lambda_{\text{eph}} < \lambda_{c2}$ regime.

In a scenario where $\lambda_{\text{eph}} = 0 = M$, the Hall conductivity shows plateaus (but with small kinks on the plateaus due to the presence of the distorted FB) as long as the Fermi level lies in between the bulk gap [43]. However, in our case (with $\lambda_{\text{eph}} \neq 0$ and $M \neq 0$), the nature of the Hall conductivity deviates significantly as there exists a cumulative effect arising from the interplay of the three parameters, namely the Fermi energy (E_f), the mass term (M) and the e-ph coupling strength (λ_{eph}). The reason for the plateaus to become tinier can be explained with the help of the bulk spectra, which are mainly

affected by M and λ_{eph} for different α values. It is understandable that a significant width of the plateau is dependent on how accurately we fix the Fermi level in the bulk gap. As discussed in Sec. III A, the individual bulk bands shrink due to the Holstein factor [Eq. (8)], and the whole band structure shifts vertically down by the polaron shift energy ($\lambda_{\text{eph}}^2 \hbar \omega_0$). Due to the band narrowing caused by the Holstein factor, the gap between the distorted (because of the Haldane term, λ) FB and VB decreases, makes it difficult for the Fermi level to lie ‘properly’ in between the bulk gap, making the plateaus less prominent, especially for higher values of λ_{eph} . Additionally, we find that the increase in σ_{xy} as a function of E_f can be explained as follows. As observed in Sec. III A, M breaks the valley degeneracy and the interplay between M and λ_{eph} renders contrasting behavior of the bulk bands at two valleys, that is, well-gapped at one valley and almost gapless at the other for $\lambda_{\text{eph}} < \lambda_c$. As E_f is increased, it is possible that at one valley, E_f may lie well in the gap, while it may lie in the CB as well at the other valley, which will contribute to higher σ_{xy} . The unusual behavior of the Hall conductivity due to the presence of a distorted FB has also been reported by Singh *et al.* [56] (in the absence of e-ph coupling). Certainly, all of the above discussions become unimportant for $\lambda_{\text{eph}} > \lambda_c$.

Interestingly, for $\alpha = 0.8$, the quantized (tiny) Hall plateaus in Fig. 18(d) are located at e^2/h (where, $|C| = 1$) and $2e^2/h$ (where, $|C| = 2$) for $\lambda_{c1} < \lambda_{\text{eph}} < \lambda_{c2}$ (shown for $\lambda_{\text{eph}} = 0.3$ and 0.4 , denoted by solid blue and black, respectively) and $0 \leq \lambda_{\text{eph}} < \lambda_{c1}$ regimes (shown for $\lambda_{\text{eph}} = 0.1$, denoted by solid green), respectively, confirm existence of two distinct topological insulating phases with a nonzero σ_{xy} (also true for any α in $0.75 \lesssim \alpha < 1$ regime), while these plateaus vanish beyond λ_{c2} , ascertaining emergence of a trivial insulating phase ($C = 0$) with $\sigma_{xy} = 0$. Thus the polaronic Hall conductivity ensures that the system undergoes a transition from a nontrivial insulating phase with quantized plateaus at $|C|e^2/h$ in the $\lambda_{\text{eph}} \lesssim \lambda_c$ regime to a trivial insulating phase with zero Hall conductivity in the $\lambda_{\text{eph}} > \lambda_c$ regime.

IV. CONCLUSION

To summarize, we have studied the effect of e-ph interaction on inducing a topological phase transition in a Haldane-Holstein model on an α - T_3 lattice. The NN and the complex NNN Haldane hopping amplitudes get renormalized by the Holstein reduction factor showing the signature of polaron formation in the system. The cases of our study are majorly divided into two scenarios, namely lower to intermediate α ($0 < \alpha \leq 0.6$) and higher ($0.6 < \alpha < 1$) values of α . With the help of the effective Hamiltonian in \mathbf{k} space, we have computed the bulk and the edge spectra where it is observed that for the first case, as we increase the e-ph coupling strength λ_{eph} , the bulk gap between the flat and valance bands closes at a critical coupling strength, namely λ_c at one K valley and reopens beyond λ_c . This feature explains that the system is characterized by two distinct insulating states below and above $\lambda_{\text{eph}} = \lambda_c$. Consequently, the conducting edge modes emerge in the $\lambda_{\text{eph}} < \lambda_c$ regime, which are preserved up to $\lambda_{\text{eph}} = \lambda_c$, and disappear for $\lambda_{\text{eph}} > \lambda_c$, signifying a topologically nontrivial to trivial phase transition. In the second case, we encounter a different scenario where the flat and valance

bands in the bulk remain gapless for the $0.65 \lesssim \alpha \lesssim 0.75$ regime and gapped for $0.75 \lesssim \alpha < 1$, till λ_{eph} reaches a first critical value, namely λ_{c_1} and become gapped till λ_{eph} assumes another critical value, namely λ_{c_2} where similar gap closing transition takes place. The explicit emergence of conducting edge modes in the $\lambda_{c_1} < \lambda_{\text{eph}} < \lambda_{c_2}$ regime both for $0.65 \lesssim \alpha \lesssim 0.75$ and $0.75 \lesssim \alpha < 1$, and also in $0 \leq \lambda_{\text{eph}} < \lambda_{c_1}$ regime for $0.75 \lesssim \alpha < 1$ that traverse through the FB around the K and K' valleys makes the latter case more intriguing. It indicates that for $0.65 \lesssim \alpha \lesssim 0.75$ ($0.75 \lesssim \alpha < 1$), the system re-enters from a conventional (topological) SM phase (in the $\lambda_{\text{eph}} < \lambda_{c_1}$ regime) to a (another) topological one (in the $\lambda_{c_1} < \lambda_{\text{eph}} < \lambda_{c_2}$ regime) upon tuning the e-ph coupling strength. The above discussions for both the cases, either with a unique λ_c or with two λ_c s, namely λ_{c_1} and λ_{c_2} , strongly indicate possibilities of inducing topological phase transition via e-ph coupling in an α - T_3 Haldane-Holstein model. Furthermore, we have numerically computed the Berry curvature and the topological invariant, namely the (polaronic) Chern number (C), for different values of α . In our study, the evidence of a discontinuous change in C from $|C| = 1$ to $|C| = 0$ for $0 < \alpha \lesssim 0.75$ regime, and from $|C| = 2$ to $|C| = 1$ and finally to $|C| = 0$ for $0.75 \lesssim \alpha < 1$ regime exhibiting a jump in the C vs λ_{eph} diagram at different critical values of the e-ph coupling for different values of α directly confirms the topological phase transition solely caused by the e-ph interaction, while interpolating α between corresponding lattice structures of graphene to a dice lattice. More specifically, the system under investigation possesses a topological insulating phase accompanied by $|C| = 1$ or $|C| = 2$ (depending on the range of α) below certain critical values of the e-ph coupling strength, and becomes a trivial insulator ($C = 0$) above the critical point. We, furthermore, incorporate the above observations in a phase diagram plotted for C in the $\lambda_{\text{eph}} - \alpha$ plane. To confirm such phases, and phase transitions from one phase to another, we have calculated the Hall conductivity for a few values of α (both small and large) as a function of λ_{eph} . The existence (vanishing) of Hall plateaus at $|C|e^2/h$ below (above) a certain critical λ_c for a particular value of α further substantiates the evidence of topological phase transitions

induced by e-ph coupling in our α - T_3 Haldane-Holstein model. We have also explored the possibility of charge ordering in our system and infer that a CDW phase is only feasible at large values of e-ph coupling, thereby precluding any possibility of the coexistence of topological and charge ordered phases. We wish to motivate that our study may serve as a powerful tool for understanding the interaction-driven topology in novel quantum systems.

ACKNOWLEDGMENTS

K.B. sincerely thanks IIT Guwahati for providing financial support through the Institute Post Doctoral Fellowship (Ref. No. IITG/R&D/IPDF/2023-24/20231003P537). M.I. and K.B. also sincerely acknowledge S. Lahiri and S. Mondal for fruitful discussions. The authors sincerely thank the anonymous referees for their valuable comments and suggestions.

APPENDIX: DERIVATION OF THE MODIFIED HALDANE-HOLSTEIN HAMILTONIAN FOR AN α - T_3 LATTICE

In this section, we briefly derive the major steps to obtain the Hamiltonian [Eq. (4) of Sec. II B] modified by the e-ph coupling, employing LFT via the generator of the transformation mentioned in Eq. (3). The transformed Hamiltonian in Eq. (2) can equivalently be expressed by the Baker-Campbell-Hausdorff formula as

$$\begin{aligned} \tilde{\mathcal{H}} &= e^R \mathcal{H} e^{-R} = \mathcal{H} + [R, \mathcal{H}] + \frac{1}{2!} [R, [R, \mathcal{H}]] \\ &+ \frac{1}{3!} [R, [R, [R, \mathcal{H}]]] + \dots \end{aligned} \quad (\text{A1})$$

Let us label the terms of Hamiltonian (1) as $\mathcal{H}^{(1)}, \mathcal{H}^{(2)}, \dots$, etc. for the first till the seventh term of Hamiltonian (1), respectively. Now, we transform each individual term as in the following. Combining the NN ($\langle \dots \rangle$) terms that are symbolized as $\mathcal{H}^{(1)}$ and $\mathcal{H}^{(2)}$ we can calculate the commutator for $\mathcal{H}^{(12)} \equiv \mathcal{H}^{(1)} + \mathcal{H}^{(2)}$ as

$$[R, \mathcal{H}^{(12)}] = \left[\lambda_{\text{eph}} \sum_i c_i^\dagger c_i (b_i^\dagger - b_i), \left[-t \sum_{\langle i', j' \rangle} c_{i'}^\dagger c_{j'} - \alpha t \sum_{\langle j', k' \rangle} c_{j'}^\dagger c_{k'} \right] \right] = -(1 + \alpha)t \sum_{i, \delta} c_i^\dagger c_{i+\delta} [\lambda_{\text{eph}} [(b_i^\dagger - b_i) - (b_{i+\delta}^\dagger - b_{i+\delta})]], \quad (\text{A2})$$

and consequently the successive commutators can be obtained as

$$[R, [R, \mathcal{H}^{(12)}]] = -(1 + \alpha)t \sum_{i, \delta} c_i^\dagger c_{i+\delta} [X_i - X_{i+\delta}]^2, \quad [R, [R, [R, \mathcal{H}^{(12)}]]] = -(1 + \alpha)t \sum_{i, \delta} c_i^\dagger c_{i+\delta} [X_i - X_{i+\delta}]^3. \quad (\text{A3})$$

where $X_i \equiv \lambda_{\text{eph}}(b_i^\dagger - b_i)$ and δ is the NN index, that is, $j = i + \delta$. Therefore, collecting terms in Eqs. (A2) and (A3) and using Eq. (A1), the NN terms are transformed as

$$\tilde{\mathcal{H}}^{(12)} = -(1 + \alpha)t \sum_{i, \delta} c_i^\dagger c_{i+\delta} \left[1 + [X_i - X_{i+\delta}] + \frac{1}{2!} [X_i - X_{i+\delta}]^2 + \frac{1}{3!} [X_i - X_{i+\delta}]^3 + \dots \right] = -(1 + \alpha)t \sum_{i, \delta} c_i^\dagger c_{i+\delta} e^{[X_i - X_{i+\delta}]}. \quad (\text{A4})$$

The NNN ($\langle \langle \dots \rangle \rangle$) Haldane terms denoted by $\mathcal{H}^{(3)}$ and $\mathcal{H}^{(4)}$ can be transformed in a similar fashion with the NNN index, η as

$$\tilde{\mathcal{H}}^{(34)} = -(1 + \alpha) \frac{\lambda}{3\sqrt{3}} \sum_{i, \eta} c_i^\dagger c_{i+\eta} e^{[X_i - X_{i+\eta}]} e^{i\phi_{i, i+\eta}}, \quad (\text{A5})$$

while the onsite mass term, $\mathcal{H}^{(5)}(\equiv \sum_i c_i^\dagger M S_z c_i)$ remains unchanged by the transformation, that is,

$$\tilde{\mathcal{H}}^{(5)} = \sum_i c_i^\dagger M S_z c_i. \quad (\text{A6})$$

The phonon energy, $\mathcal{H}^{(6)}(\equiv \hbar\omega_0 \sum_i b_i^\dagger b_i)$ and the e-ph interaction term, $\mathcal{H}^{(7)}(\equiv \lambda_{\text{eph}} \hbar\omega_0 \sum_i c_i^\dagger c_i (b_i^\dagger + b_i))$ can respectively be transformed by Eq. (A1) as

$$\tilde{\mathcal{H}}^{(6)} = \hbar\omega_0 \sum_i [b_i^\dagger b_i - \lambda_{\text{eph}} c_i^\dagger c_i (b_i^\dagger + b_i) + \lambda_{\text{eph}}^2 c_i^\dagger c_i], \quad (\text{A7})$$

$$\tilde{\mathcal{H}}^{(7)} = \hbar\omega_0 \sum_i [\lambda_{\text{eph}} c_i^\dagger c_i (b_i^\dagger + b_i) - 2\lambda_{\text{eph}}^2 c_i^\dagger c_i], \quad (\text{A8})$$

where in Eqs. (A7) and (A8), we have used the identity, namely, $n_i^2 = n_i(\equiv c_i^\dagger c_i)$ for the fermionic number operator. Hence, summing Eqs. (A4)–(A8), we obtain Eq. (4).

-
- [1] M. Z. Hasan and C. L. Kane, *Rev. Mod. Phys.* **82**, 3045 (2010).
[2] X.-L. Qi and S.-C. Zhang, *Rev. Mod. Phys.* **83**, 1057 (2011).
[3] D. J. Thouless, M. Kohmoto, M. P. Nightingale, and M. den Nijs, *Phys. Rev. Lett.* **49**, 405 (1982).
[4] K. von Klitzing, *Rev. Mod. Phys.* **58**, 519 (1986).
[5] C. L. Kane and E. J. Mele, *Phys. Rev. Lett.* **95**, 226801 (2005).
[6] B. A. Bernevig, T. L. Hughes, and S.-C. Zhang, *Science* **314**, 1757 (2006).
[7] J. E. Moore and L. Balents, *Phys. Rev. B* **75**, 121306(R) (2007).
[8] L. Fu, C. L. Kane, and E. J. Mele, *Phys. Rev. Lett.* **98**, 106803 (2007).
[9] M. König, S. Wiedmann, C. Brüne, A. Roth, H. Buhmann, L. W. Molenkamp, X.-L. Qi, and S.-C. Zhang, *Science* **318**, 766 (2007).
[10] D. Hsieh, D. Qian, L. Wray, Y. Xia, Y. S. Hor, R. J. Cava, and M. Z. Hasan, *Nature (London)* **452**, 970 (2008).
[11] B. Yan and C. Felser, *Annu. Rev. Condens. Matter Phys.* **8**, 337 (2017).
[12] N. P. Armitage, E. J. Mele, and A. Vishwanath, *Rev. Mod. Phys.* **90**, 015001 (2018).
[13] Y. Tanaka, M. Sato, and N. Nagaosa, *J. Phys. Soc. Jpn.* **81**, 011013 (2012).
[14] J. M. Kosterlitz and D. J. Thouless, *J. Phys. C: Solid State Phys.* **6**, 1181 (1973).
[15] T. Senthil, *Annu. Rev. Condens. Matter Phys.* **6**, 299 (2015).
[16] N. Nagaosa, J. Sinova, S. Onoda, A. H. MacDonald, and N. P. Ong, *Rev. Mod. Phys.* **82**, 1539 (2010).
[17] C.-Z. Chang, J. Zhang, X. Feng, J. Shen, Z. Zhang, M. Guo, K. Li, Y. Ou, P. Wei, L.-L. Wang, Z.-Q. Ji, Y. Feng, S. Ji, X. Chen, J. Jia, X. Dai, Z. Fang, S.-C. Zhang, K. He, Y. Wang *et al.*, *Science* **340**, 167 (2013).
[18] C.-Z. Chang, W. Zhao, D. Y. Kim, H. Zhang, B. A. Assaf, D. Heiman, S.-C. Zhang, C. Liu, M. H. W. Chan, and J. S. Moodera, *Nat. Mater.* **14**, 473 (2015).
[19] Y. Deng, Y. Yu, M. Z. Shi, Z. Guo, Z. Xu, J. Wang, X. H. Chen, and Y. Zhang, *Science* **367**, 895 (2020).
[20] F. D. M. Haldane, *Phys. Rev. Lett.* **61**, 2015 (1988).
[21] W. Beugeling, E. Kalesaki, C. Delerue, Y.-M. Niquet, D. Vanmaekelbergh, and C. M. Smith, *Nat. Commun.* **6**, 6316 (2015).
[22] H. Hu and Q. Si, *Sci. Adv.* **9**, eadg0028 (2023).
[23] Z. Huang, J. H. Wu, Y. Huang, C. Liu, C. Chen, and F. Ma, *J. Phys. D: Appl. Phys.* **55**, 045301 (2022).
[24] G.-F. Zhang, Y. Li, and C. Wu, *Phys. Rev. B* **90**, 075114 (2014).
[25] E. Tang, J.-W. Mei, and X.-G. Wen, *Phys. Rev. Lett.* **106**, 236802 (2011).
[26] S. Okamoto, N. Mohanta, E. Dagotto, and D. N. Sheng, *Commun. Phys.* **5**, 198 (2022).
[27] R. Liu, W.-C. Chen, Y.-F. Wang, and C.-D. Gong, *J. Phys.: Condens. Matter* **24**, 305602 (2012).
[28] M. Trescher and E. J. Bergholtz, *Phys. Rev. B* **86**, 241111(R) (2012).
[29] T. Andrijauskas, E. Anisimovas, M. Račiūnas, A. Mekys, V. Kudriašov, I. B. Spielman, and G. Juzeliūnas, *Phys. Rev. A* **92**, 033617 (2015).
[30] B. Jaworowski, A. Manolescu, and P. Potasz, *Phys. Rev. B* **92**, 245119 (2015).
[31] A. H. Castro Neto, F. Guinea, N. M. R. Peres, K. S. Novoselov, and A. K. Geim, *Rev. Mod. Phys.* **81**, 109 (2009).
[32] K. S. Novoselov, A. K. Geim, S. V. Morozov, D. Jiang, Y. Zhang, S. V. Dubonos, I. V. Grigorieva, and A. A. Firsov, *Science* **306**, 666 (2004).
[33] B. Sutherland, *Phys. Rev. B* **34**, 5208 (1986).
[34] J. Vidal, R. Mosseri, and B. Douçot, *Phys. Rev. Lett.* **81**, 5888 (1998).
[35] Y. Xu and L.-M. Duan, *Phys. Rev. B* **96**, 155301 (2017).
[36] D. F. Urban, D. Bercioux, M. Wimmer, and W. Häusler, *Phys. Rev. B* **84**, 115136 (2011).
[37] D. Bercioux, N. Goldman, and D. F. Urban, *Phys. Rev. A* **83**, 023609 (2011).
[38] J. D. Malcolm and E. J. Nicol, *Phys. Rev. B* **93**, 165433 (2016).
[39] M. Vigh, L. Oroszlány, S. Vajna, P. San-Jose, G. Dávid, J. Cserti, and B. Dóra, *Phys. Rev. B* **88**, 161413(R) (2013).
[40] D. Bercioux, D. F. Urban, H. Grabert, and W. Häusler, *Phys. Rev. A* **80**, 063603 (2009).
[41] F. Wang and Y. Ran, *Phys. Rev. B* **84**, 241103(R) (2011).
[42] B. Dey, P. Kapri, O. Pal, and T. K. Ghosh, *Phys. Rev. B* **101**, 235406 (2020).
[43] S. Mondal and S. Basu, *Phys. Rev. B* **107**, 035421 (2023).

- [44] R. Soni, N. Kaushal, S. Okamoto, and E. Dagotto, *Phys. Rev. B* **102**, 045105 (2020).
- [45] N. Mohanta, R. Soni, S. Okamoto, and E. Dagotto, *Commun. Phys.* **6**, 240 (2023).
- [46] A. Raoux, M. Morigi, J.-N. Fuchs, F. Piéchon, and G. Montambaux, *Phys. Rev. Lett.* **112**, 026402 (2014).
- [47] J. D. Malcolm and E. J. Nicol, *Phys. Rev. B* **92**, 035118 (2015).
- [48] E. Illes, J. P. Carbotte, and E. J. Nicol, *Phys. Rev. B* **92**, 245410 (2015).
- [49] J. Wang and J.-F. Liu, *Phys. Rev. B* **103**, 075419 (2021).
- [50] J. J. Wang, S. Liu, J. Wang, and J.-F. Liu, *Phys. Rev. B* **102**, 235414 (2020).
- [51] A. D. Kovács, G. Dávid, B. Dóra, and J. Cserti, *Phys. Rev. B* **95**, 035414 (2017).
- [52] S. K. F. Islam and P. Dutta, *Phys. Rev. B* **96**, 045418 (2017).
- [53] E. Illes and E. J. Nicol, *Phys. Rev. B* **95**, 235432 (2017).
- [54] T. Biswas and T. K. Ghosh, *J. Phys.: Condens. Matter* **28**, 495302 (2016).
- [55] T. Biswas and T. K. Ghosh, *J. Phys.: Condens. Matter* **30**, 075301 (2018).
- [56] A. Singh and G. Sharma, *Phys. Rev. B* **107**, 245150 (2023).
- [57] E. V. Gorbar, V. P. Gusynin, and D. O. Oriekhov, *Phys. Rev. B* **99**, 155124 (2019).
- [58] Y.-R. Chen, Y. Xu, J. Wang, J.-F. Liu, and Z. Ma, *Phys. Rev. B* **99**, 045420 (2019).
- [59] E. Illes and E. J. Nicol, *Phys. Rev. B* **94**, 125435 (2016).
- [60] L. Chen, J. Zuber, Z. Ma, and C. Zhang, *Phys. Rev. B* **100**, 035440 (2019).
- [61] O. Roslyak, G. Gumbs, A. Balassis, and H. Elsayed, *Phys. Rev. B* **103**, 075418 (2021).
- [62] A. Balassis, D. Dahal, G. Gumbs, A. Iurov, D. Huang, and O. Roslyak, *J. Phys.: Condens. Matter* **32**, 485301 (2020).
- [63] J. Wang, J. F. Liu, and C. S. Ting, *Phys. Rev. B* **101**, 205420 (2020).
- [64] C.-D. Han and Y.-C. Lai, *Phys. Rev. B* **105**, 155405 (2022).
- [65] J. Sun, T. Liu, Y. Du, and H. Guo, *Phys. Rev. B* **106**, 155417 (2022).
- [66] A. Iurov, L. Zhemchuzhna, G. Gumbs, D. Huang, D. Dahal, and Y. Abranyos, *Phys. Rev. B* **105**, 245414 (2022).
- [67] A. Iurov, G. Gumbs, and D. Huang, *J. Phys.: Condens. Matter* **32**, 415303 (2020).
- [68] A. Singh and G. Sharma, *Phys. Rev. B* **108**, 195426 (2023).
- [69] M. Islam, T. Biswas, and S. Basu, *Phys. Rev. B* **108**, 085423 (2023).
- [70] M. Islam and P. Kapri, *J. Phys.: Condens. Matter* **35**, 105301 (2023).
- [71] B. Dey and T. K. Ghosh, *Phys. Rev. B* **98**, 075422 (2018).
- [72] B. Dey and T. K. Ghosh, *Phys. Rev. B* **99**, 205429 (2019).
- [73] M. A. Mojarro, V. G. Ibarra-Sierra, J. C. Sandoval-Santana, R. Carrillo-Bastos, and G. G. Naumis, *Phys. Rev. B* **101**, 165305 (2020).
- [74] Z. P. Niu and S. J. Wang, *J. Phys. D: Appl. Phys.* **55**, 255303 (2022).
- [75] L. Tamang, T. Nag, and T. Biswas, *Phys. Rev. B* **104**, 174308 (2021).
- [76] L. Tamang and T. Biswas, *Phys. Rev. B* **107**, 085408 (2023).
- [77] A. Iurov, G. Gumbs, and D. Huang, *Phys. Rev. B* **99**, 205135 (2019).
- [78] B. Bradlyn, L. Elcoro, J. Cano, M. G. Vergniory, Z. Wang, C. Felser, M. I. Aroyo, and B. A. Bernevig, *Nature (London)* **547**, 298 (2017).
- [79] S. Rachel, *Rep. Prog. Phys.* **81**, 116501 (2018).
- [80] A. S. Sørensen, E. Demler, and M. D. Lukin, *Phys. Rev. Lett.* **94**, 086803 (2005).
- [81] S. Raghu, X.-L. Qi, C. Honerkamp, and S.-C. Zhang, *Phys. Rev. Lett.* **100**, 156401 (2008).
- [82] M. Hohenadler and F. F. Assaad, *J. Phys.: Condens. Matter* **25**, 143201 (2013).
- [83] C. Wang, A. C. Potter, and T. Senthil, *Science* **343**, 629 (2014).
- [84] K. Sun, H. Yao, E. Fradkin, and S. A. Kivelson, *Phys. Rev. Lett.* **103**, 046811 (2009).
- [85] C. N. Varney, K. Sun, M. Rigol, and V. Galitski, *Phys. Rev. B* **82**, 115125 (2010).
- [86] X.-Y. Dong, A. G. Grushin, J. Motruk, and F. Pollmann, *Phys. Rev. Lett.* **121**, 086401 (2018).
- [87] C. Repellin, T. Yefsah, and A. Sterdyniak, *Phys. Rev. B* **96**, 161111(R) (2017).
- [88] S. Julià-Farré, M. Müller, M. Lewenstein, and A. Dauphin, *Phys. Rev. Lett.* **125**, 240601 (2020).
- [89] J. T. Devreese and A. S. Alexandrov, *Rep. Prog. Phys.* **72**, 066501 (2009).
- [90] A. S. Alexandrov and J. T. Devreese, *Advances in Polaron Physics* (Springer Heidelberg, Heidelberg, 2010).
- [91] A. Chatterjee and S. Mukhopadhyay, *Polarons and Bipolarons: An Introduction*, 1st ed. (CRC Press, Boca Raton, FL, 2017).
- [92] M. Tinkham, *Introduction to Superconductivity*, 2nd ed. (Dover Publications, New York, 2004).
- [93] H. Fröhlich, *Phys. Rev.* **79**, 845 (1950).
- [94] J. Bardeen, *Rev. Mod. Phys.* **23**, 261 (1951).
- [95] J. Ziman, *Electrons and Phonons: The Theory of Transport Phenomena in Solids* (Oxford University Press, London, 2001).
- [96] J.-A. Yan, R. Stein, D. M. Schaefer, X.-Q. Wang, and M. Y. Chou, *Phys. Rev. B* **88**, 121403(R) (2013).
- [97] G. G. Samsonidze, E. B. Barros, R. Saito, J. Jiang, G. Dresselhaus, and M. S. Dresselhaus, *Phys. Rev. B* **75**, 155420 (2007).
- [98] S. Mukhopadhyay and A. Chatterjee, *Phys. Lett. A* **204**, 411 (1995).
- [99] S. Mukhopadhyay and A. Chatterjee, *Phys. Rev. B* **59**, R7833 (1999).
- [100] L. Challis, *Electron-Phonon Interactions in Low-Dimensional Structures* (Oxford University Press, London, 2003).
- [101] S. Kivelson and D. Hone, *Phys. Rev. B* **28**, 4833 (1983).
- [102] J. R. Senna and S. Das Sarma, *Phys. Rev. B* **48**, 4552 (1993).
- [103] K. Luo and X. Dai, *Phys. Rev. X* **13**, 011027 (2023).
- [104] L. Zhang, U. Bhattacharya, A. Bachtold, S. Forstner, M. Lewenstein, F. Pistolesi, and T. Grass, *npj Quantum Inf.* **9**, 7 (2023).
- [105] Y.-X. Zhang, W.-T. Chiu, N. C. Costa, G. G. Batrouni, and R. T. Scalettar, *Phys. Rev. Lett.* **122**, 077602 (2019).
- [106] O. Bradley, G. G. Batrouni, and R. T. Scalettar, *Phys. Rev. B* **103**, 235104 (2021).
- [107] H. Tan, Y. Liu, Z. Wang, and B. Yan, *Phys. Rev. Lett.* **127**, 046401 (2021).
- [108] M. V. Araújo, J. P. de Lima, S. Sorella, and N. C. Costa, *Phys. Rev. B* **105**, 165103 (2022).

- [109] Y. Xie, Y. Li, P. Bourges, A. Ivanov, Z. Ye, J.-X. Yin, M. Z. Hasan, A. Luo, Y. Yao, Z. Wang, G. Xu, and P. Dai, *Phys. Rev. B* **105**, L140501 (2022).
- [110] M. Campetella, G. Marini, J. S. Zhou, and M. Calandra, *Phys. Rev. B* **108**, 024304 (2023).
- [111] H. Miao, T. T. Zhang, H. X. Li, G. Fabbris, A. H. Said, R. Tartaglia, T. Yilmaz, E. Vescovo, J.-X. Yin, S. Murakami, X. L. Feng, K. Jiang, X. L. Wu, A. F. Wang, S. Okamoto, Y. L. Wang, and H. N. Lee, *Nat. Commun.* **13**, 273 (2022).
- [112] H. Miao, T. T. Zhang, H. X. Li, G. Fabbris, A. H. Said, R. Tartaglia, T. Yilmaz, E. Vescovo, J.-X. Yin, S. Murakami, X. L. Feng, K. Jiang, X. L. Wu, A. F. Wang, S. Okamoto, Y. L. Wang, and H. N. Lee, *Nat. Commun.* **14**, 6183 (2023).
- [113] M. Casebolt, C. Feng, R. T. Scalettar, S. Johnston, and G. G. Batrouni, [arXiv:2403.15386](https://arxiv.org/abs/2403.15386) [cond-mat.str-el].
- [114] M. Koschorreck, D. Pertot, E. Vogt, B. Fröhlich, M. Feld, and M. Köhl, *Nature (London)* **485**, 619 (2012).
- [115] C. Kohstall, M. Zaccanti, M. Jag, A. Trenkwalder, P. Massignan, G. M. Bruun, F. Schreck, and R. Grimm, *Nature (London)* **485**, 615 (2012).
- [116] A. Schirotzek, C.-H. Wu, A. Sommer, and M. W. Zwierlein, *Phys. Rev. Lett.* **102**, 230402 (2009).
- [117] F. Scazza, G. Valtolina, P. Massignan, A. Recati, A. Amico, A. Burchianti, C. Fort, M. Inguscio, M. Zaccanti, and G. Roati, *Phys. Rev. Lett.* **118**, 083602 (2017).
- [118] I. Garate, *Phys. Rev. Lett.* **110**, 046402 (2013).
- [119] Z. Li and J. P. Carbotte, *Phys. Rev. B* **88**, 195133 (2013).
- [120] Z. Li and J. P. Carbotte, *Eur. Phys. J. B* **88**, 87 (2015).
- [121] R. Heid, I. Y. Sklyadneva, and E. V. Chulkov, *Sci. Rep.* **7**, 1095 (2017).
- [122] N. Mostaan, N. Goldman, and F. Grusdt, [arXiv:2305.00835](https://arxiv.org/abs/2305.00835) [cond-mat.quant-gas].
- [123] R. Schmidt and T. Enss, *SciPost Phys.* **13**, 054 (2022).
- [124] M.-G. Hu, M. J. Van de Graaff, D. Kedar, J. P. Corson, E. A. Cornell, and D. S. Jin, *Phys. Rev. Lett.* **117**, 055301 (2016).
- [125] N. B. Jørgensen, L. Wacker, K. T. Skalmstang, M. M. Parish, J. Levinsen, R. S. Christensen, G. M. Bruun, and J. J. Arlt, *Phys. Rev. Lett.* **117**, 055302 (2016).
- [126] S. Chaudhary, A. Haim, Y. Peng, and G. Refael, *Phys. Rev. Res.* **2**, 043431 (2020).
- [127] H. Hübener, U. De Giovannini, and A. Rubio, *Nano Lett.* **18**, 1535 (2018).
- [128] T. Holstein, *Ann. Phys.* **8**, 343 (1959).
- [129] J. Bonča, S. A. Trugman, and I. Batistić, *Phys. Rev. B* **60**, 1633 (1999).
- [130] L. M. Cangemi, A. S. Mishchenko, N. Nagaosa, V. Cataudella, and G. D. Filippis, *Phys. Rev. Lett.* **123**, 046401 (2019).
- [131] A. Camacho-Guardian, N. Goldman, P. Massignan, and G. M. Bruun, *Phys. Rev. B* **99**, 081105(R) (2019).
- [132] H. L. Calvo, J. S. Luna, V. Dal Lago, and L. E. F. Foa Torres, *Phys. Rev. B* **98**, 035423 (2018).
- [133] S. Li, L.-H. Hu, R.-X. Zhang, and S. Okamoto, *Commun. Phys.* **6**, 235 (2023).
- [134] D. Pimenov, A. Camacho-Guardian, N. Goldman, P. Massignan, G. M. Bruun, and M. Goldstein, *Phys. Rev. B* **103**, 245106 (2021).
- [135] J. Medina Dueñas, H. L. Calvo, and L. E. F. Foa Torres, *Phys. Rev. Lett.* **128**, 066801 (2022).
- [136] C. Lu, M. Zhang, H. Wang, Q. Ai, and T. Liu, *Phys. Rev. B* **107**, 125118 (2023).
- [137] I. G. Lang and Y. A. Firsov, *Sov. Phys. JETP* **16**, 1301 (1963).
- [138] M. W. Alam, B. Souayah, and S. F. Islam, *J. Phys.: Condens. Matter* **31**, 485303 (2019).